Use of hyperspectral sounders to retrieve daytime sea-surface temperature from mid-infrared radiances: Application to IASI

V Capelle, J.-M Hartmann

Use of hyperspectral sounders to retrieve daytime sea-surface temperature from mid-infrared radiances: Application to IASI

V. Capelle[#] and J.-M. Hartmann

Laboratoire de Météorologie Dynamique/IPSL, CNRS, École polytechnique, Institut polytechnique de Paris, Sorbonne Université, École normale supérieure, PSL Research University, F-91120 Palaiseau, France.

[#]Corresponding author: virginie.capelle@lmd.ipsl.fr

Highlights

- SST retrievals using daytime spectra from the infrared hyperspectral sounder IASI
- Successful use of mid-infrared wavelengths despite large contributions of solar light.
- High consistency and accuracy of the temperatures retrieved from wavelengths between 3.6 to 4.0 μm.

Keywords

Sea surface skin temperature ; Infrared radiative transfer retrieval algorithm ; Infrared Atmospheric Sounder Interferometer (IASI) ; Solar contribution ; Mid-infrared wavelengths

Abstract: We propose a physically-based methodology for sea-surface skin-temperature (SST) retrievals from daytime spectra recorded by the hyperspectral Infrared Atmospheric Sounding Interferometer (IASI). The approach, which takes sun light into account, minimizes the differences between measured and computed radiances at numerous points within two windows centered near 3.7 and 4.0 μm. We demonstrate that, even when the solar contribution is large, with brightness temperatures increased by several tens of kelvin at the shortest wavelengths, very consistent SSTs are retrieved in both windows. Furthermore, the values obtained are, after correction for the cool-skin

effect, in excellent agreement (<0.05 K on average) with the in-situ measurements of the depth temperature provided by nearby drifters. This opens renewed perspectives for daytime SST determinations from space, since the IASI mid-infrared windows used here provide SSTs that are, with respect to those retrieved around 9 and 11 μm, much less sensitive to errors in the computed radiative contribution of water vapor.

1. Introduction

The importance of precisely knowing the sea-surface skin temperature (SST) and the efforts made for its determination having been extensively discussed previously, the interested reader is invited to consult e.g. (Robinson, 2010 ; Martin, 2014 ; Minnett et al., 2019). Recall that, in the framework of climate monitoring, one needs to detect and quantify small regional or global SST changes lower than 0.2 K/decade (see e.g. Ohring et al., 2005 ; Merchant et al., 2008 and 2012). For that purpose, the key requirements for a climate SST record and the associated difficulties often encountered, which have been discussed in detail in Capelle et al. (2022) and references therein, are: (i) an accuracy < 0.1 K and a stability <0.05 K/decade, (ii) a high homogeneity of long time series (15 years at minimum, for which assuring the continuity between sensors is often challenging), (iii) an independency from any model or other SST product (such as in-situ measurements or other datasets) and, finally, (iv) the highest achievable sensitivity to SST changes, the main difficulty being here to correctly take into account the effects of the water vapor content of the atmosphere. Simultaneously satisfying all these requirements is generally difficult, as it is the case for the majority of available SST products which are derived using 2 or 3 wavelengths only, with retrieval algorithms generally based on regressions from in-situ buoys or ships measurements, either in the infrared (AVHRR, MODIS, etc..) or microwave (AMRS-E). In addition to the long term monitoring of the SST, another important issue is to know the diurnal variations, a key information in a variety of contexts including the Diurnal Temperature Range issue, remote sensing, ocean and climate modeling, and air-sea heat and gas fluxes estimates (Stuart-Menteth et al., 2003 ; Bernie et al., 2007 ; Kawai and Wada, 2007 ; Clayson and Bogdanoff, 2013 ; Morak-Bozzo et al., 2016 ; Ruzmaikin et al., 2017).

Within this framework, SST products derived from radiances collected by Earth-polar orbiting satellites offer only a partial observation of the diurnal cycle due to their only two overpasses per day, and to the fact that retrievals cannot be made under cloudy or dusty conditions for infrared sounders or under heavy precipitation for microwave ones. However, they may provide reference inputs for the improvement of climatic and oceanic models, since they complement the data provided by the buoys network by offering a more complete spatio-temporal sampling (Merchant et al., 2019). Collocating satellite observations with in-situ measurements at different local times may improve the modeling of

the diurnal variations of the near-surface thermal structure, but this requires an equal quality of the SST restitution for both day- and night-time. This latter constraint is particularly challenging since solar light may significantly contribute to mid-infrared radiances collected from space when looking down to the surface, increasing observed brightness temperatures below 4 μm by several tens of kelvin, as shown below and in Chen et al. (2013). Given the uncertainty in the modeling of the solar contribution, this explains why practically all satellite-based daytime SST retrievals in the infrared use radiances around 9-12 μm, even though the instrument provides data at shorter wavelengths (e.g.: Walton et al., 1998 ; O'Carroll et al., 2012 ; Kilpatrick et al., 2015 ; Merchant et al., 2019 ; Minnett et al., 2019). A good example is given by MODIS observations, with which nighttime SSTs are deduced from measurements around 3.75, 3.96, 4.05, 11.0, and 12.0 μm, while only the last two wavelengths are used in the treatment of daytime data (Kilpatrick et al., 2015). However recall the noticeable exception of Merchant et al. (2009b) where the 11 and 3.9 μm channels were used to retrieved daytime SSTs from the Geostationary Operational Environmental Satellite 12. In this study, the radiances for the short wavelength were treated by removing, in order to obtain "pseudonighttime" data, the associated solar contribution. The latter was computed in a way quite similar to that used in the present study, but due to uncertainties on its prediction, only those measurements for which the solar photons raise the brightness temperature by less than 1 K at 3.9 μm were retained (which is not the case in our study, thanks to the availability of many mid-infrared channels in IASI spectra). Let us finally mention a study (Liu et al., 2014) in which a method is proposed to remove the solar contribution from the data at 3.7 μm provided by the Visible Infrared Imaging Radiometer Suite by using the radiances recorded at 1.6 and 2.25 μm. Finally, it is important to recall that using only long wavelengths leads to a lower accuracy of the SST retrieved from nighttime observations since the atmosphere is less transparent around 10 μm than in the mid infrared, which induces errors principally linked to the water vapor content of the atmosphere (Capelle et al., 2022). This is particularly important in regions with high atmospheric humidity, as it is the case in Tropics [see e.g. (Merchant et al., 2009a) for AVHRR, (Kilpatrick et al., 2015) for MODIS, (Embury et al., 2012) for AATSR, (Tsamalis and Saunders, 2018) for CCI ATSR SST].

In Capelle et al. (2022), we used nighttime observations from the Infrared Atmospheric Sounding Interferometer, IASI (Hilton et al., 2012), in order to retrieve SSTs, using a physically-based radiative-transfer model, from radiances within atmospheric-transparency windows. The main results of that study, are threefold: (i) While systematic biases due to errors in the modeling of the radiative contribution of water vapor (resulting from spectroscopic and/or atmospheric-state knowledge errors) may significantly affect the SSTs retrieved around 9 and 11 μm (and to a lesser extent those at 4.7 μm), it is not the case for the windows centered at 3.7 and 4.0 μm. (ii) Despite the significant radiometric noise at these short wavelengths of the IASI spectra (Serio et al., 2018), the latter provide SSTs which are, after correction for the cool-skin effect [e.g. (Saunders, 1967 ; Fairall et al., 1996)], in excellent agreement with nearby (in time and position) in-situ depth-temperature measurements, with a mean difference lower than 0.05 K and a robust standard deviation of 0.25 K. (iii) The comparisons made with in-situ measurements for the 2008-2020 Metop-A period have enabled to demonstrate the excellent stability of the time series, with a trend of the satellite minus in-situ temperature difference lower than 0.05 K/decade. The consistency between the three generations of IASI on-board Metop-A, -B, and -C have also been verified by comparing their monthly-averaged 1°x1° grids SSTs over their overlap periods (2013–2020 for Metop-A and Metop-B, and 2019–2020 for Metop-C), leading to a mean SST difference lower than 0.02 K , with a SD of 0.3 K consistent with the natural variation of the SST within a month. Altogether, these results satisfy the prerequisites enumerated above when considering SST time series as a climate data record. This opens promising perspectives by demonstrating the possibility to provide an accurate, as well as stable, SST time-series from IASI over the planned 20 years of the Metops-suite, that will be followed by two more decades of the IASI-New Generation missions (Crevoisier et al., 2014). Furthermore, these achievements and the discussion made above show that and extension, beyond nighttime, of the study by Capelle et al. (2022) is desirable and of interest.

This paper generalizes the study of Capelle et al. (2022) to IASI daytime near-nadir observations by including the solar contribution in the radiative-transfer model. The main objective of this methodology study is to demonstrate that, thanks to the availability of a large number of spectral channels highly sensitive to surface temperature, the radiances around 3.7 and 4.0 μm enable accurate

SST determinations provided that the solar contribution is correctly taken into account. Recall that the IASI level2 SSTs are derived from an empirical orthogonal-function regression, using the principal component scores of the first two bands (August et al., 2012), disregarding the information brought by short wavelengths of the spectra. The theoretical model and input data used are presented in Sec. 2. The IASI spectra retained and the procedure for their analysis are the subjects of Sec. 3, the results being discussed in Sec. 4 before some concluding remarks (Sec. 5). Note that we here propose and validate a methodology and that analyses of SST long time series, as done in Capelle et al. (2022), is beyond the scope of the present paper.

2. Theoretical model and data used

2.1 Theoretical model

For the observing geometry schematized in Fig. 1, the expression used to compute (and fit) the IASI radiance (W/m^2/str/cm^{-1}) at wave number σ (cm^{-1}) is:

$$I_{\text{Theo}}(\sigma,\theta_I,\varphi_I,\theta_S,\varphi_S,T_{\text{Surf}}) = I_{\text{Surf}}(\sigma,\theta_I,T_{\text{Surf}}) + I_{\text{Atm\_up}}(\sigma,\theta_I) + I_{\text{Atm\_down}}(\sigma,\theta_I) + I_{\text{Sun}}(\sigma,\theta_I,\varphi_I,\theta_S,\varphi_S) \quad (1)$$

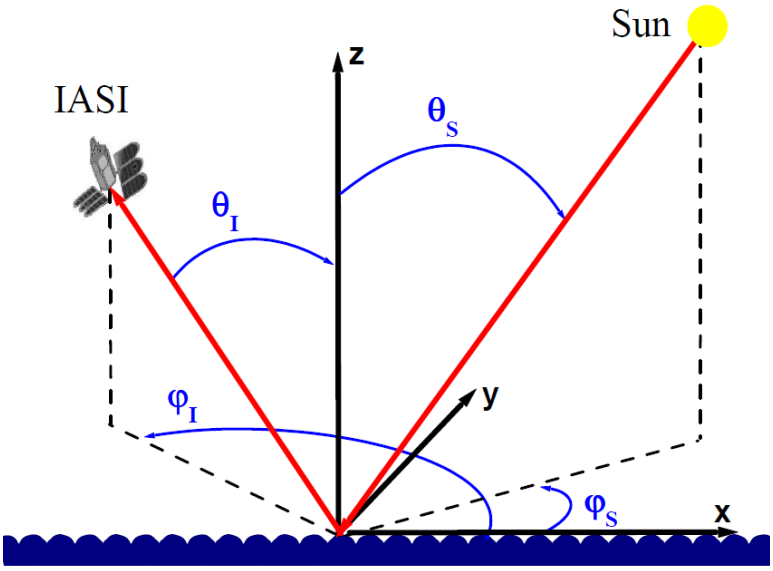

Fig. 1: Observation geometry. The $\vec{z}$ axis is along the local vertical, $\vec{x}$ points toward the south and $\vec{y}$ toward the east.

In this equation, which disregards any scattering of light in the atmosphere, the first term is the emission by the surface transmitted up to the instrument. Assuming (see Sec. 2.2) that the sea-surface directional emissivity $\varepsilon(\sigma,\theta_I)$ does not depend on the SST (T_{Surf}), and since both this emissivity and the black-body radiance $I_{BB}(\sigma,T_{Surf})$ are constant over the narrow instrument function $F_{Inst}(\Delta\sigma)$ of IASI, I_{Surf} is given by:

$$I_{Surf}(\sigma,\theta_I,T_{Surf}) = \varepsilon(\sigma,\theta_I)\overline{\tau}(\sigma,\theta_I)I_{BB}(\sigma,T_{Surf}) \ , \quad (2)$$

with

$$\overline{\tau}(\sigma,\theta_I) = \int_{-\infty}^{+\infty} F_{Inst}(\sigma-\sigma')\exp\left[-\int_0^{z_{Inst}} \alpha(\sigma',z)dz/\cos(\theta_I)\right]d\sigma' \ , \quad (3)$$

where z_{Inst} is the altitude of IASI, and $\alpha(\sigma,z)$ denotes the atmospheric absorption coefficient at altitude z.

Using the same notations, the second term in Eq. (1), representing the emission of the atmospheric column between the surface and the instrument, is given by:

$$I_{Atm\_up}(\sigma,\theta_I) = \int_{-\infty}^{+\infty} F_{Inst}(\sigma-\sigma')\int_0^{z_{Inst}} I_{Loc}(\sigma',z,\theta_I)dz/\cos(\theta_I)d\sigma' \ , \quad (4)$$

with

$$I_{Loc}(\sigma',z,\theta_I) = I_{BB}[\sigma',T(z)]\alpha(\sigma',z)\exp\left[-\int_z^{z_{Inst}} \alpha(\sigma',z')dz'/\cos(\theta_I)\right] \ . \quad (5)$$

The third term in Eq. (1) is the emission of the atmosphere toward the surface that is then reflected and transmitted up to the instrument. Rigorously speaking, it involves an integration over all possible downward-emission directions, each weighted by the proper (which ensures that the considered light is redirected within the IASI field of view) bi-directional reflectivity. Since the probability of the latter depends on the wind-dependent wave-slope distribution and because an angular integration must be made, a correct calculation of $I_{Atm\_down}(\sigma,\theta_I)$ for each treated IASI spectrum is extremely costly. In order to avoid doing so, we first carried simplified calculations corresponding to the extreme cases of Lambertian and specular reflectances, respectively [note that these are close to the limit cases of the sea surface for very high and low wind conditions, respectively (Watts et al., 1996)], and treated a

limited but representative set of IASI spectra. The first case can be correctly predicted by considering a single path with and elevation angle of θ_{down} =53° (Turner, 2004), while the second also considers a single elevation angle $\theta_{down} = \theta_I$, now identical to that of the IASI pointing. One thus has:

$$I_{Atm\_down}(\sigma,\theta_I) = \int_{-\infty}^{+\infty} F_{Inst}(\sigma-\sigma') \int_0^{+\infty} I_{Loc'}(\sigma', z, \theta_{down}) dz / \cos(\theta_{down}) d\sigma' , \quad (6)$$

with

$$I_{Loc'}(\sigma', z, \theta_{down}) = \left[1-\varepsilon(\sigma',\theta_I)\right] \exp\left[-\int_0^{z_{Inst}} \alpha(\sigma', z') dz' / \cos(\theta_I)\right] \times I_{BB}[\sigma', T(z)] \alpha(\sigma', z) \exp\left[-\int_0^{z} \alpha(\sigma', z') dz' / \cos(\theta_{down})\right] . \quad (7)$$

The results of our tests show that the mean difference between the SSTs obtained using the specular and Lambertian assumptions is of typically +0.025 K, a weak difference which could be expected from the smallness of both the atmospheric absorption and sea water reflectance, regardless of the water vapor content of the involved atmosphere. Considering that this value is ten times smaller than the standard deviation, that using the fixed value θ_{down} =53° independently of the IASI pointing is technically simpler, and by consistency with what was done in the analysis of nighttime spectra (Cappelle et al., 2022), we have retained this choice for the final processing of all the spectra.

Finally, the solar contribution, $I_{Sun}(\sigma,\theta_I,\varphi_I,\theta_S,\varphi_S)$, is written as:

$$I_{Sun}(\sigma,\theta_I,\varphi_I,\theta_S,\varphi_S) = A(\theta_I,\varphi_I,\theta_S,\varphi_S) \rho(\sigma,\theta_I,\varphi_I,\theta_S,\varphi_S) \cos(\theta_S) d\Omega_S \times \int_{-\infty}^{+\infty} F_{Inst}(\sigma-\sigma') I^0_{Sun}(\sigma') \exp\left[-\int_0^{z_{Inst}} \alpha(\sigma',z) dz/\cos(\theta_I)\right] \exp\left[-\int_0^{+\infty} \alpha(\sigma',z) dz/\cos(\theta_S)\right] d\sigma' , \quad (8)$$

where $I^0_{Sun}(\sigma)$, $d\Omega_S$, and $\rho(\sigma,\theta_I,\varphi_I,\theta_S,\varphi_S)$ respectively denote the (disk-averaged) radiance emitted by the sun, the solid angle within which the sun is seen from Earth, and the bi-directional spectral reflectivity of the surface. The factor $A(\theta_I,\varphi_I,\theta_S,\varphi_S)$ includes the probability for waves to have a slope enabling solar photons coming along the (θ_S,φ_S) direction to be redirected toward the instrument (along θ_I,φ_I) after a specular reflection. Its value can be computed (as discussed in Sec. 4.1) from knowledge of the observation geometry and of the wind direction and speed. However, since its prediction carries uncertainties (Zhang and Wang, 2010 ; Liang et al., 2010) that may bias the

retrieved SSTs, this quantity is below considered as an unknown to be fitted in the analysis of the spectra.

Most of the terms participating to Eqs. (1)-(8) can be computed from knowledge of the sea water optical constants, as well as of the thermodynamic conditions of each observed scene (i.e. the vertical profiles of temperature, pressure, …), and molecular absorption data feeding the calculation of the absorption coefficient. Since all these input data can be determined upstream independently (see Sec. 2.2), the theoretical radiance thus involves two unknowns only: $A(\theta_I,\varphi_I,\theta_S,\varphi_S)$, through $I_{Sun}(...)$ in Eq. (8), and T_{Surf}, through $I_{BB}(\sigma,T_{Surf})$ in Eq. (2). Their values were retrieved from fits of IASI spectra as explained in Sec. 3.2.

2.2 Input data and computational tools used.

The sea-surface emissivity $\varepsilon(\sigma,\theta_I)$ was computed, following Masuda et al. (1988), using the complex index of refraction for pure water of Downing and Williams (1975), after a shifting of +4cm^{-1} and an increase of the real part by +6 10^{-3} (Friedman, 1969) in order to take salinity effects into account. The small (Newman et al., 2005 ; Masuda, 2008), or unknown, dependence of $\varepsilon(\sigma,\theta_I)$ on the SST was disregarded and, since we consider observations close to nadir ($|\theta_I|$<30°), the weak (Masuda et al., 1988) influence of the wind speed was neglected. The reflectivity $\rho(\sigma,\theta_I,\varphi_I,\theta_S,\varphi_S)$ was computed (see Appendix A) using Fresnel's coefficients, Snell's law, and the complex index of refraction mentioned above. In the 3.6 to 4.0 μm region used for the final retrievals, the solar radiance was represented by a Planck function with a temperature of 5657 K compatible with Platnick and Fontenla (2008). Note that the sensitivities of the results to the index of refraction and solar spectrum are discussed in Appendix B which also validates the input data retained. As done by Capelle et al. (2022) and Hartmann et al. (2018), the absorption coefficients were computed, for each atmospheric state (see below), using the 4AOP code (Scott and Chédin, 1981 ; Cheruy et al., 1995). The spectroscopic parameters for the individual lines of absorbing gases were taken from the GEISA database (Jacquinet-Husson et al., 2016), complemented by the MT_CKD (version 3.1) parameterization (Mlawer et al., 2012) of the water-vapor continuum, and the collision-induced

absorption by N_2 as well as CO_2 line-wing corrections were implemented as in Hartmann et al. (2018). Local Thermodynamic Equilibrium (LTE) was assumed, an approximation which breaks down for the populations of some molecular vibrational levels at elevated altitude (Ĺopez-Puertas and Taylor, 2001). However, non-LTE only affects the atmospheric emission close to the centers of intense absorption bands [e.g. near 4.3 μm for CO_2 (DeSouza-Machado et al., 2007 ; Chen et al., 2013)], regions disregarded in the present study which, contrariwise, uses transparency windows where the atmospheric transmission is high (see Sec. 3.2).

The calculations of the atmospheric absorptions, transmissions and emissions require knowledge of the altitude-dependent state (temperature, pressure, volume mixing ratios of the absorbing species) of the atmosphere probed by each IASI observation. Here, the temperature and water profiles are determined independently, as in Capelle et al. (2022), using a proximity recognition in brightness temperature (BT) within the Thermodynamic Initial Guess Retrieval (TIGR) climatological database (Chédin et al., 1985 ; Chevallier et al., 1998). For all of the atmospheric situations in TIGR, BTs are computed with the radiative transfer model (4A/OP) for a set of 8 channels, carefully selected principally in the 13-14 μm spectral band, and then compared with the corresponding observed IASI BTs. The channels used are principally sensitive to the temperature and water profiles with relatively small contributions from other gases, the surface or the sun [see also (Capelle et al., 2012) for a complete description].

The wind speed and direction needed for the calculation of the solar parameter *A* come from interpolation of the hourly 0.25°x0.25° resolution European Centre for Medium-Range Weather Forecasts' (ECMWF) 5th Re-Analysis (ERA5) dataset (Hersbach and Dee, 2016).

3. The IASI spectra and their treatment

3.1 Selected IASI spectra

In order to validate the methodology proposed in this paper, a limited but nonetheless sufficiently large set of 99010 IASI Metop-A daytime observations was used. These spectra, recorded between 2015 and 2019, were selected using the following criteria: (i) Only cloud- and aerosol-free

observations were retained, selected by using criteria on brightness temperatures from IASI and the collocated AVHRR instrument, as explained in Capelle et al. (2022). As in this latter study, the largest dust-contaminated observations that may remain after the cloud-aerosol filtering are removed by retrieving the dust optical depth (DAOD) at 10 μm using the method described in Capelle et al. (2018). For nighttime spectra, every observation with a DAOD>0.03 was eliminated in Cappelle et al. (2022). For daytime observations, to avoid any contamination by the solar contribution in the DAOD retrievals (which is based on the use of channels not only in the range 8-12 μm, but also around 4.7 μm), only the observations with a DAOD>0.2 are eliminated. These limit values have been chosen empirically. (ii) We only kept those IASI spectra for which an in-situ depth-temperature measurement, made from a drifter close to the observed sea spot in both localization (< 20 km away) and time (< 3 h difference, 98.8% of them being within 1 h difference), is available from the NOAA in-situ Quality Monitor (IQUAM; https://www.star.nesdis.noaa.gov/socd/sst/iquam/) (Xu and Ignatov, 2014). (iii) Data collected for $|\theta_I|$>30° were disregarded in order to minimize potential biases resulting from the dependence of the sea-surface emissivity on wind speed (Masuda et al., 1988). Note that the selected set includes recordings made for a large variety of atmospheric-humidity conditions, with total precipitable water contents between 0.2 and 6.7 cm.

3.2 Analysis procedure

In the treatment of the observations, some of the spectral channels of locally minimum absorption selected by Capelle et al. (2022) were used. We here only retained the two windows of highest frequencies: W_4, with 107 points from 2480 to 2528 cm^{-1} and W_5, with 185 points from 2594 to 2760 cm^{-1}. Following the conclusions of Capelle et al. (2022), the longer wavelengths (W_1 around 11 μm ; W_2 around 9.0 μm ; W_3 around 4.7 μm) were not used given their too large sensitivities to errors in the computation of the (poorly known) contribution of water vapor as well as in the sea-surface emissivity and atmospheric temperature profile. These sensitivities, analyzed in Appendix A of Capelle et al. (2022), result from the larger contribution of the water vapor continuum and weaker

dependence of the blackbody function on temperature at long wavelengths when compared to short ones. The analysis of each spectrum used three steps.

Step 1: The retained measured radiances were simultaneously fitted using Eqs. (1)-(8), floating $A(\theta_I,\varphi_I,\theta_S,\varphi_S)$ and $\overline{T}_{Surf}$ in order to minimize the mean deviation, over all channels inside windows W_4 and W_5, between the measured and computed radiances, i.e. the quantity: $\sum_{\sigma_i \in W_4 \,\&\, W_5}\left[I_{Theo}(\sigma_i, A, \overline{T}_{Surf}) - I_{IASI}(\sigma_i)\right]^2$. It is important to emphasize that this procedure is made possible by the hyperspectral character of IASI [which is not the case for MODIS (Kilpatrick et al., 2015) and GOES-12 (Merchant et al., 2009), for instance] and the associated availability of numerous channels in a wavelength region over which the solar spectrum shows important relative variations and may significantly contribute to the measured radiances.

Step 2: The value of $A(\theta_I,\varphi_I,\theta_S,\varphi_S)$ was then fixed, and $T_{Surf}(\sigma_i)$ was retrieved, for all selected channels σ_i, by solving the equation $I_{Theo}[\sigma_i, A, T_{Surf}(\sigma_i)] = I_{IASI}(\sigma_i)$. Setting A to zero in this exercise yields SST values "as if it were nighttime" since the solar photons collected by the instrument are then disregarded. For a preliminary test of steps 1 and 2, we selected a spectrum showing a significant solar contribution and collected over a dry atmosphere, and used all the (five) windows retained for the treatment of nighttime observations (Capelle et al., 2022). Figure 2 exemplifies the results obtained and shows that, for the analyzed observation, the effect of solar light is obvious in W_4 and W_5 while it is negligible in W_1 and W_2, a result explained by the fact that $I^0_{Sun}(\sigma)/I_{BB}(\sigma, T_{Surf})$ increases exponentially with σ and varies by more than three orders of magnitude from the lowest (~830 cm^{-1}) to the highest (~2760 cm^{-1}) wave number. Figure 2 also demonstrates that, in contrast to the treatment disregarding sun light (using A=0), taking the latter into account provides SSTs that are consistent throughout the entire spectral range. Note that the increase of the IASI noise with σ (Serio et al., 2018) is responsible for the corresponding increase of the scatter of $T_{Surf}(\sigma)$, an effect further amplified when the sun contribution is large. Indeed, in the case of Fig. 2, the radiance due to solar photons represents, near 2600 cm^{-1}, more than half of the signal collected by IASI which, after its

removal, increases the scatter of $T_{\mathrm{Surf}}(\sigma_i)$ by a factor of about two, explaining the greater dispersion of the red points when compared to the blue ones.

Step 3: Finally, for the further analyses of the consistency of the SSTs retrieved in different spectral windows $\mathrm{W_k}$, we from now on consider the averages:

$$\overline{T}_{\mathrm{k}} = \overline{T}_{\mathrm{Surf}}(\mathrm{W_k}) = \sum_{\sigma_i \in \mathrm{W_k}} T_{\mathrm{Surf}}(\sigma_i)/N_{\mathrm{k}}\,, \qquad (9)$$

where N_{k} is the number of data points inside $\mathrm{W_k}$ (see example in the insert of Fig. 2).

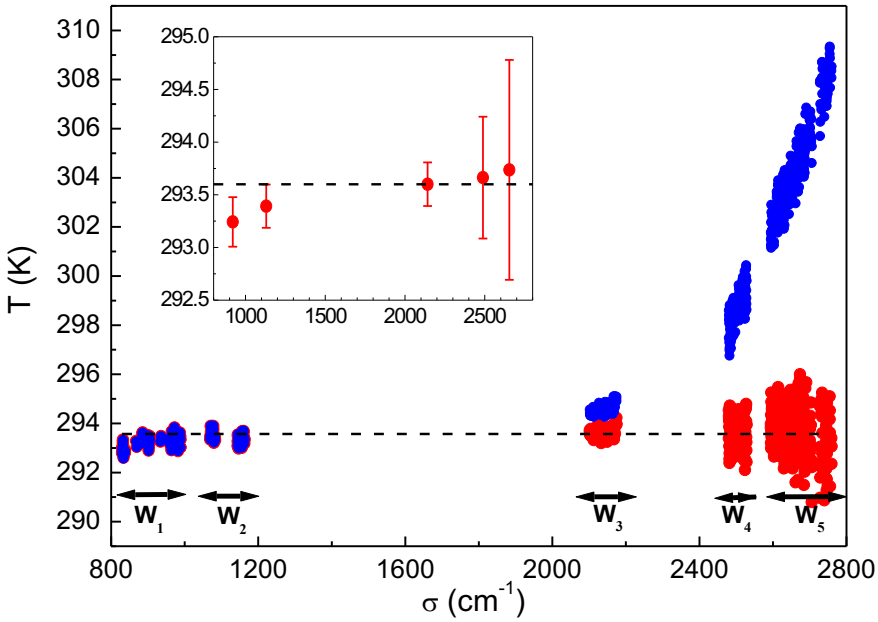

Fig. 2: Main panel: SSTs retrieved by taking into account (red circles) and disregarding (blue circles) the solar contribution. The horizontal dashed line represents the average of all red circles. Insert: Averages, $\overline{T}_{\mathrm{k}}$ [see Eq. (9)], of the temperatures $T_{\mathrm{Surf}}(\sigma_i)$ retrieved in each window $\mathrm{W_k}$ by taking the solar light into account (the error bars represent the standard deviation), the horizontal dashed line denoting the uncertainty-weighted average.

4. Results and discussion

4.1 The solar parameter *A*

In many of the observations the solar contribution, and thus also the retrieved A_{Fit} parameter, is small, except when the instrument points close to the sun glint which, for the geometry of Fig. 1,

corresponds to small values of both $\theta_I - \theta_S$ and $\varphi_I - \varphi_S$. Since the IASI orbits are close to the South-North axis, the swath practically follows the East-West direction and, for the retained observations close to nadir, θ_I hence varies between 0° and 30° while φ_I is close to 90° (Eastward pointing) or 270° (Westward pointing). The local time of all observations being 9:30 AM at the Equator, the sun is in the East, implying that a large solar contribution may only be collected on this side of the swath and when the sun azimuth angle φ_S is close to 90°. According to this last criterion, large values of A_{Fit} will be obtained during the winter at moderate south latitudes only, because the sun inclination to the South is too large (i.e. φ_S is significantly smaller than 90°) in the Northern hemisphere, the situation being reversed in the summer. All these considerations are confirmed by the maps in Fig. 3, which corresponds to the orbits of July 16 and January 25 in 2018.

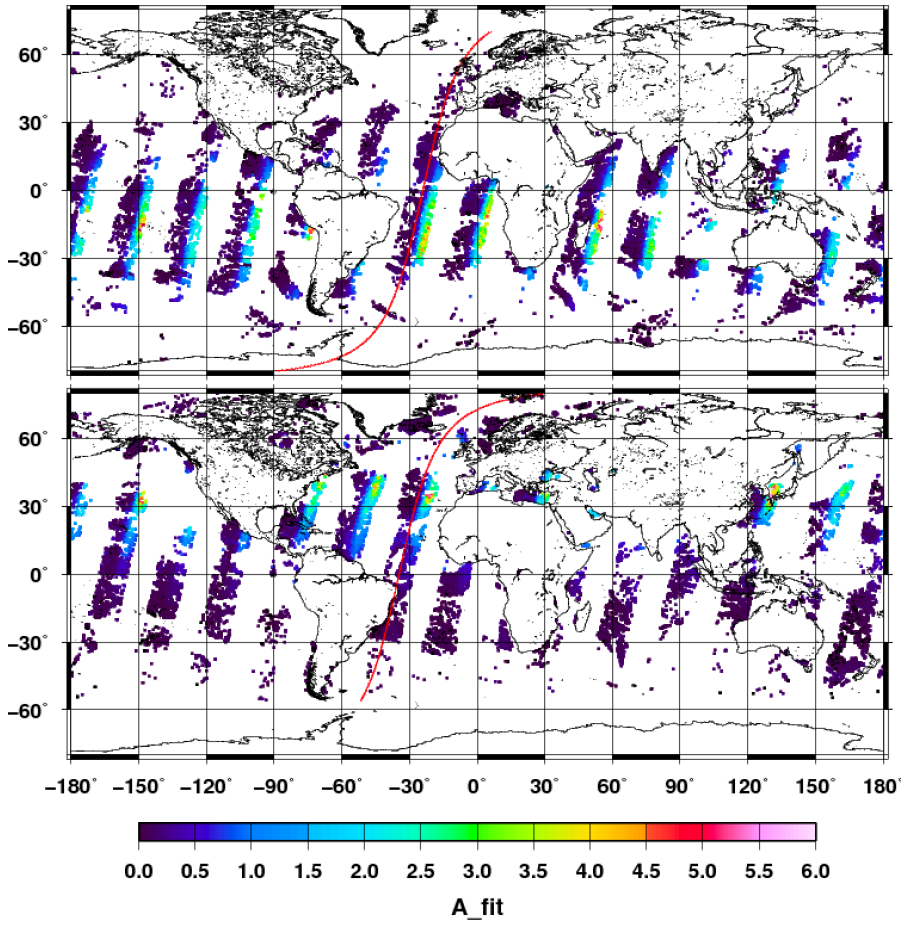

Fig. 3: Color maps of the values of the solar parameter retrieved from the IASI spectra collected along the 2018 orbits of January 25 (top panel) and July 16 (lower panel). The red line on the central orbits indicates the center of the swath (nadir pointing).

Now, before discussing the SSTs, a first validation of the proposed methodology is performed by assessing the quality of the retrieved solar parameter by comparison with predictions based on two parameterizations of the probability of wave slopes (Cox and Munk, 1954 ; Bréon and Henriot, 2006) calculated from knowledge of the geometry of the observation and of the wind direction and speed (see Appendix C). The fitted (A_{Fit}) and theoretical (A_{Theo}) values for every IASI observation treated in this study are compared in Fig. 4 (where 99.45% of the points satisfy $|A_{Fit}-A_{Theo}| \leq 1$). Note that, in this plot, we have retained only those results associated with observations for which the wave-tilt angle θ_W [see Eq. (A8) of Appendix C] is smaller than 25° since this is the limit of reliability of the above mentioned models. As can be seen, the retrieved and predicted values are very consistent, the best linear fit of the data in Fig. 4 leading (with close results for the two models of A_{Theo}) to a slope of 0.9, an offset of 0.09, and a correlation value of 0.97. The insert, displaying the corresponding scatter density plot obtained for the parametrization of (Bréon and Henriot, 2006), indicates that the maximum of density is centered on the best linear fit, with the majority of situations corresponding to small values of A_{Theo} (as it can be expected from Fig. 3) The density plot for the parametrization of (Cox and Munk, 1954) gives a similar pattern (not shown). Furthermore, the deviations with respect to $A_{Fit}=A_{Theo}$ are practically within the combined uncertainties of our determinations, indicated by error bars on the plot, and of the theoretical models, estimated from the uncertainties on the wave-slope probability-law parameters given by Cox and Munk (1954) and Bréon and Henriot (2006) as being about 0.2 and 0.08, respectively. These results provide a first validation of the procedure proposed here. Note that, although the blue symbols in Fig. 4 seem slightly less scattered than the red ones, concluding that the most recent facet model (Bréon and Henriot, 2006) would be the best remains hazardous due to uncertainties and to the limited number of observations (about 10^5) considered here. Furthermore recall that the comparisons in Fig. 4 are only presented for a first validation of our method and that the present paper focuses on its test from the point of view of the SST. An evaluation of the wave-slope models is thus beyond the scope of this study, but this issue is currently under investigation and will be adressed in a forthcoming study considering much more IASI observations.

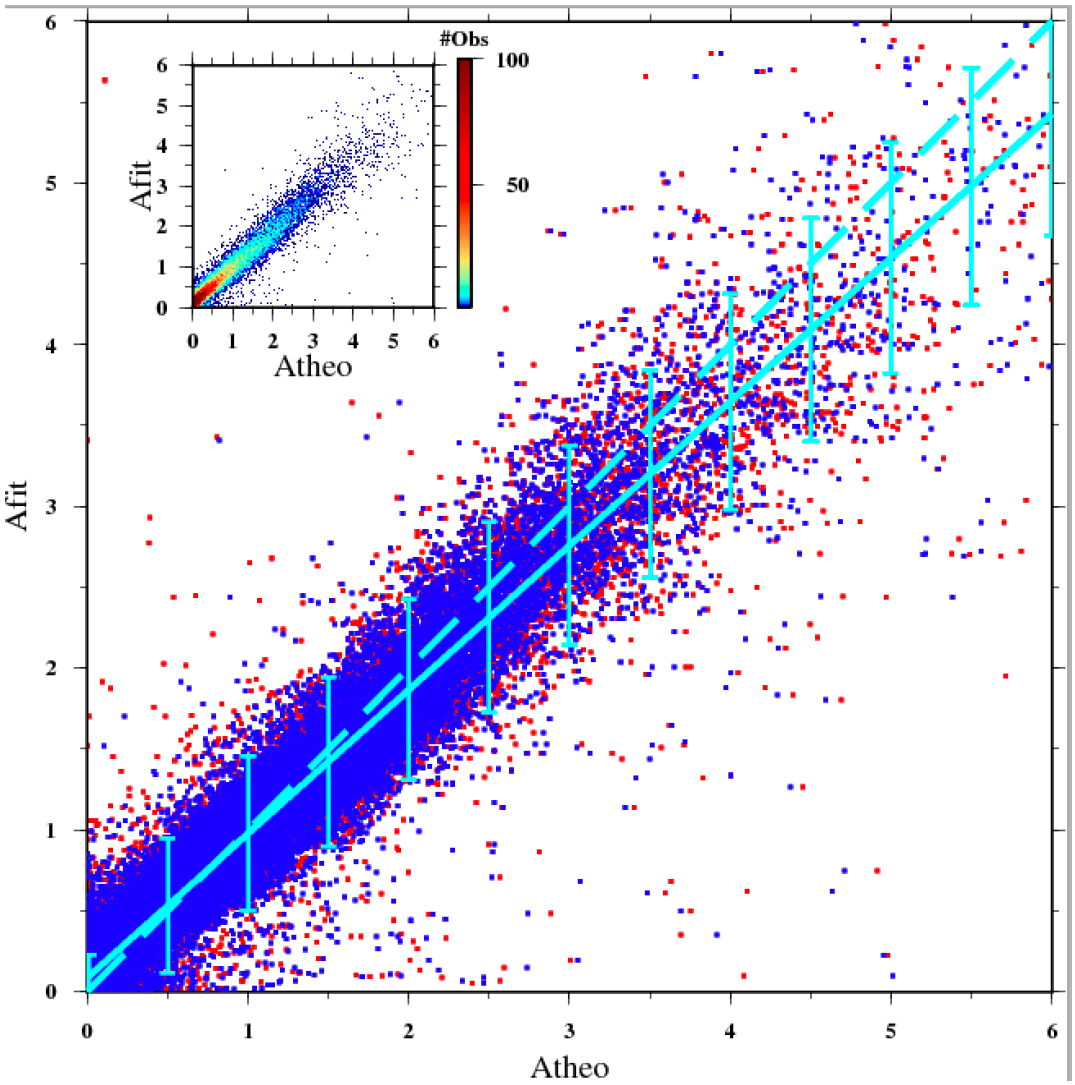

Fig. 4: Comparison between the A_{Fit} parameters obtained from fits of IASI spectra with those, A_{Theo}, calculated (see Appendix C) for each observation (provided that the wave-tilt angle is smaller than 25°) by using the parameterizations of Cox and Munk (1954) (red circles) and of Bréon and Henriot (2006) (blue circles), and the wind speed and direction provided by ECMWF (see Sec. 2.2 and Appendix C). The cyan error bars on A_{Fit} represent the one sigma statistical one from the least-square fit. The full and dashed cyan lines represent the best linear fit and the A_{Fit}=A_{Theo} law, respectively. Insert: corresponding scatter density plot for boxes of 0.03x0.03 obtained for the parameterizations of Bréon and Henriot (2006).

4.2 The SSTs

We now focus on the validation of the retrieved sea-surface (skin) temperatures. For that purpose, the averaged values $\overline{T}_4$ and $\overline{T}_5$ [Eq. (9)] obtained from the 3.7 and 4.0 windows are

compared with in-situ measurements from drifters (Sec. 3.1). The latter provide the "depth temperature" T_{Depth}, measured typically 20 cm below the surface, while $\overline{T}_{k=4,5}$ are representative of the "skin temperature" T_{Skin}, corresponding to few micrometers below the surface. In order to directly compare them, a model representing their theoretical differences ($\Delta T = T_{\mathrm{Skin}} - T_{\mathrm{Depth}}$) is thus needed. During night, a "cool-skin effect" around -0.2 K is observed and predicted (Saunders, 1967 ; Fairall et al., 1996 ; Donlon et al., 2002 ; Minnett et al., 2011), which was taken into account in Capelle et al. (2022) using the approach proposed by Fairall et al. (1996), forced by the surface fluxes and the friction velocity provided by the European Centre for Medium-Range Weather Forecasts (ECMWF) model ERA5 forecast data (Hersbach et al., 2018 and 2020) with sea-water thermophysical properties from web.mit.edu/seawater (Sharqawy et al., 2010; Nayar et al., 2016). During the day, this effect is slightly reduced by the heating due to the absorption of a portion of the solar flux within the ocean skin layer. In order to compute ΔT, we used Eq. (14) of Fairall et al. (1996), updated as described by Wick et al. (2005). Finally, under slow-wind conditions, the solar heating may also induce a warming that decreases with depth but may be significant near the surface, leading to a thermal stratification in the upper layer of the ocean. This effect was taken into account using the simple parameterization described in Zeng and Beljaars (2005). Altogether, the skin-to-depth corrections used here are similar to those applied in the ECMWF model and described in (ECMWF, 2016). It must be emphasized that these parameterizations are not exact, a statement which particularly applies to that of the warm layer since it is based on a too simple thermal stratification. In addition, they depend on ERA5 surface fluxes, which are not observations, but models. The skin-to-depth conversion is therefore not expected to be fully accurate, in particular for slow wind and high insolation conditions, where the warm layer effect is not negligible.

In the following, statistics for the differences $\Delta T_5 \equiv \overline{T}_5 - T_{\mathrm{Depth}}$ obtained from IASI spectra in window W_5 are discussed, expressed in terms of the median (M) and robust standard deviation (RSD) , defined as 1.5 times the Median Absolute Deviation, i.e. the median of all the absolute difference between each individuals points and the median of the population (e.g. Rousseeuw and Hubert, 2011), instead of the mean (Mean) and standard deviation (STD), as often done in SST analyses, in order to

attenuate the effect of outliers due to unscreened clouds or to errors in the measurement [see (Capelle et al., 2022) and references therein]. They are complemented by considering the double difference $\delta\Delta T_5 \equiv \Delta T_5 - \Delta T_{\mathrm{Theo}}$, where ΔT_{Theo} denotes the value of the skin-to-depth temperature difference computed for each observation as explained above, all the results, including those for ΔT_4 and $\delta\Delta T_4$, being summarized in Table 1 where the nighttime results from Capelle et al. (2022) are recalled.

	All colloc (99010)				**A_{Theo}< 0.5 (81458 colloc)**				**A_{Theo}>1 (11060 colloc)**			
	ΔT_k (K)		$\delta\Delta T_k$ (K)		ΔT_k (K)		$\delta\Delta T_k$ (K)		ΔT_k (K)		$\delta\Delta T_k$ (K)	
	k=4	k=5	k=4	k=5	k=4	k=5	k=4	k=5	k=4	k=5	k=4	k=5
Mean	-0.21 **-0.25**	-0.22 **-0.28**	0.01 **0.00**	0.00 **-0.02**	-0.21	-0.22	0.02	0.00	-0.22	-0.24	0.00	-0.02
STD	0.37 **0.37**	0.36 **0.37**	0.37 **0.37**	0.36 **0.38**	0.37	0.36	0.36	0.36	0.40	0.38	0.39	0.38
Median	-0.20 **-0.23**	-0.21 **-0.26**	0.03 **0.02**	0.02 **-0.01**	-0.20	-0.21	0.03	0.02	-0.21	-0.23	0.01	-0.01
RSD	0.30 **0.25**	0.30 **0.24**	0.30 **0.25**	0.30 **0.25**	0.30	0.29	0.29	0.29	0.35	0.34	0.35	0.33

Table 1: Statistics of the IASI (skin) versus in-situ drifter (depth) temperature differences in windows $W_{k=4}$ (around 4.0 µm) and $W_{k=5}$ (around 3.7 µm). $\Delta T_k \equiv \overline{T}_k - T_{\mathrm{Depth}}$ is the difference between the retrieved temperature $\overline{T}_k$ and the collocated in-situ measured depth temperature T_{Depth}, while $\delta\Delta T_k \equiv \Delta T_k - \Delta T_{\mathrm{Theo}}$, where ΔT_{Theo} denotes the value of the skin-to-depth temperature difference computed for each observation, as explained in Sec. 4.2, following Fairall et al. (1996), Wick et al. (2005) and Zeng and Beljaars (2005). The numbers in bold characters in columns 2 to 5 correspond to the nighttime results for the same period from Capelle et al. (2022).

399

400 The overall median temperature difference ΔT_5 obtained between IASI and the drifters for the 99010
401 collocations analyzed in the W_5 window is $M(\Delta T_5)$=-0.21 K (*RSD*=0.30 K). After correction of the
402 cool-skin effect as explained above, the corresponding values for $\delta\Delta T_5=\Delta T_5 - \Delta T_{Theo}$ are $M(\delta\Delta T_5)$=0.02
403 K (*RSD*=0.30 K). These results are close to those obtained, for the same time period, from nighttime
404 observations by Capelle et al. (2022), i.e. $M(\Delta T_{I5})$=-0.26 K (*RSD*=0.24 K) and $M(\delta\Delta T_5)$=-0.01 K
405 (*RSD*=0.25 K), respectively. As already observed for nighttime observations in Capelle et al. (2022),
406 $M(\Delta T_{IASI})$ is slightly larger than the average value generally retained for skin-to-depth temperature
407 conversion (e.g. ΔT =-0.17 K in Donlon et al. (2002); ΔT =-0.13 K in Minnett et al. (2011). However,
408 it should be emphasized that these last two numbers, obtained from shipboard measurements,
409 correspond to an asymptotic behavior reached for wind speeds larger than 8 $m.s^{-1}$, which is not
410 representative of the majority of the observations used here. For the collocations analyzed here, the
411 averaged wind speed is 6 $m.s^{-1}$, and the resulting observed depth-to-skin effect of -0.21 K is, for this
412 wind speed value, in agreement with the above mentioned studies. However, these overall statistics
413 include SSTs retrieved for observations involving a broad range of solar contributions, with spectra
414 which are close to nighttime conditions, when the instrument looks in a direction opposite to that of
415 the sun, and others that are largely affected, when the instrument points near the sun glint (see Fig. 3).
416 In order to evaluate the robustness of our procedure when the sun contribution increases, we display,
417 in Fig. 5, the evolution of the median ΔTs retrieved in windows W_4 and W_5 versus the solar parameter
418 A_{Theo}, since the latter is well adapted for this purpose. This statement is demonstrated by Fig. A2 of
419 Appendix D, where the impact of the solar contribution on the retrieved temperature $\overline{T_5}$ (i.e. the
420 difference between the value obtained using the fitted parameter A_{Fit} and that retrieved imposing
421 A_{Fit}=0) shows a strong correlation with A_{Theo}. Note that Fig. A2 also points out the potential large
422 impact of the sun on the temperature retrieval, with errors higher than 40 K when solar photons are
423 disregarded. Figure 5 shows that: (i) the retrieved ΔTs are extremely stable with A_{Theo}, with an almost
424 constant value around -0.2 K ; (ii) the values obtained using the W_4 and W_5 windows are very
425 consistent, even if their difference slightly increases with the magnitude of the solar contribution ; (iii)

the ΔTs obtained from IASI spectra are in excellent agreement with the skin-to-depth temperature differences computed as described above, implying that the absolute bias in our retrieval is very small and stable whatever the magnitude of the solar contribution. For instance, the difference between the IASI-retrieved ΔT in window W_5 and the theoretical predictions has a median $M(\delta\Delta T_5)$= 0.02 K (RSD=0.29 K) for observations with a very small solar contribution (A_{Theo}<0.5), while $M(\delta\Delta T_5)$=-0.01 K (RSD=0.33 K) when spectra significantly affected by the sun (A_{Theo}>1.0) are used (similar values are obtained for W_4 as shown by Table 1). Recalling that neglecting solar light leads (see Fig. A2 of Appendix D) to errors on $\overline{T}_5$ that vary from negligible to about 40 K along the x axis of Fig. 5, these result demonstrate the extreme robustness of the retrieval procedure proposed in this paper. It is worth noting that the SSTs obtained here from sun-contaminated spectra have, as those retrieved from nighttime observations (Capelle et al., 2022), absolute biases below the 0.1 K threshold required (Ohring et al., 2005 ; Merchant et al., 2008 ; Minnett and Corlett, 2012) for a SST product usable for climate studies.

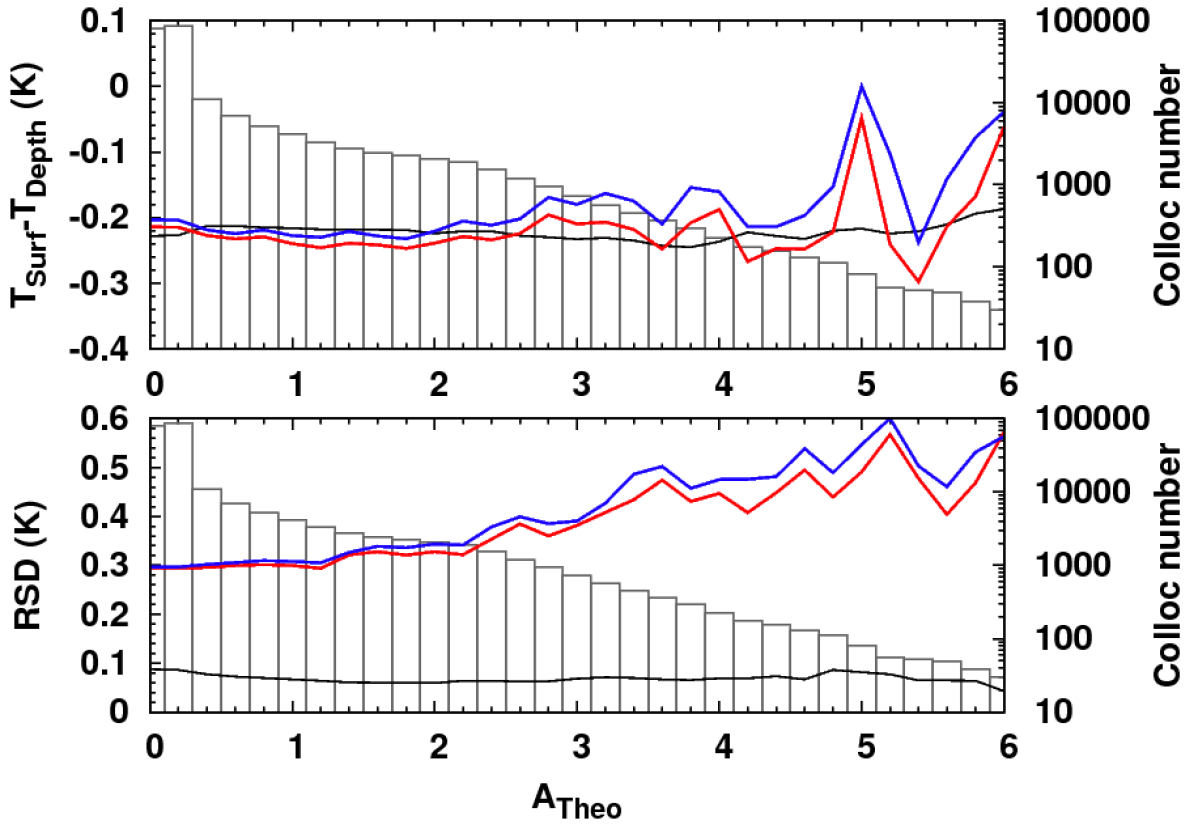

Fig. 5: Upper panel: Left y axes: Average (over all observations using a bin of ΔA_{Theo}=0.2) differences $\Delta T_{\mathrm{k}}= \overline{T}_{\mathrm{k}} - T_{\mathrm{Depth}}$ between the sea-surface skin temperatures $\overline{T}_4$ and $\overline{T}_5$ retrieved from IASI spectra in windows W_4 (blue) and W_5 (red) and the depth temperatures measured in situ, versus the theoretical value A_{Theo} of the solar parameter computed (see Appendix C) using the parameterization of Bréon and Henriot (2006). The black line represents the values of ΔT computed (see text), for the conditions of each observation, following Fairall et al. (1996), Wick et al. (2005) and Zeng and Beljaars (2005). Right y axis: Number of IASI-drifter collocations used, denoted by grey boxes in the figure. Lower panel: The RSDs associated with the above described results.

Some atmospheric situations may affect the quality of the restitutions through two main effects. Firstly, the presence of unscreened clouds tends to reduce the radiance observed by the satellite, and the retrieved SST is then underestimated. Although they are relatively rare, such cases exist in our collocations, as indicated by the slight shift toward negative values of the mean of the $\Delta T_{\mathrm{IASI}} = T_{\mathrm{IASI}} - T_{\mathrm{Depth}}$ distribution when compared to the median (see Table 1). In the 3.6-4.0 µm range, the presence of aerosols may also contaminate the restitutions, the main contributors being the mineral dusts and, to a lesser extent, the sea-salt coarse-mode which are usually confined inside the bottom part of the boundary layer to which infrared sounders are weakly sensitive (see e.g. Pierangelo et al., 2013). These aerosols may make two opposite contributions. Firstly, they reduce the radiance collected by the satellite by absorbing the radiation, leading to an underestimation of both the retrieved SST and A_{Fit} parameter. This effect is however relatively small in the mid-infrared region used here, and corresponds to an error smaller than 0.5 K (see e.g. sensitivity studies in Peyridieu et al., 2013), especially after filtering every observations with a DAOD retrieved at 10 µm lower than 0.2, as it is explained in Sec. 3.1. Secondly, in the 3.6-4.0 µm spectral range, aerosols may also act on the observed radiance by scattering the radiation, principally that coming from the sun. This increases the solar contribution to the measured spectra, leading to an overestimation of both the SST and A_{Fit}, with and impact all the more important when the collected solar flux is large. For the majority of the observations analyzed here, for which A_{Theo}<0.5, this effect is negligible (as for nighttime conditions). In contrast, for extreme cases with A_{Theo}>3, the scattering of solar light by aerosols can lead to errors on the retrieved SST of up to 3-4 kelvin and to an overestimation on A_{Fit} reaching 50%, according to

synthetic simulations (no shown) carried out for a DAOD=0.2. When analyzing the results obtained, and in particular those in Figs. 4 and 5, we conclude that such extreme cases are not so frequent in the collocations retained for this study. Indeed, in Fig. 4, no significant deviation from the linear fit is observed when A_{Theo} increases, and Fig. 5 does not indicate any large overestimation of the SST for A_{Theo} >3 when compared to he results obtained for smaller A_{Theo} values. These positive findings can be explained by the fact that the potentially large contributions of scattered solar light are due to the presence of transported mineral dust, a phenomenon which principally occurs during the summer over the Atlantic, within the "dust belt" between 0° and 30°N (Peyridieu et al., 2013), whereas the "glint situations" with large A_{Fit} values are located at higher latitude during this season (see e.g. Fig. 3). Some errors may appear in the spring where the "glint" observations are located close to the equator and some local overestimations of the SST are thus expected where dusts are then principally located [see again (Peyridieu et al., 2013)]: In the Guinean Gulf, within the "dust belt" over the Atlantic from the South-West of Africa to the North of Brazilian coats, and close to coasts in the Indian ocean. Their impact in these regions is however likely quite limited, given the small AOD and the low-altitude transport involved (Peyridieu et al., 2013 ; Yu et al., 2019). These statements are confirmed by the fact that the bias and the standard deviation in our restitutions remain practically unchanged when a more strict filtering of dusty scenes [DAOD<0.03, as it was done for nighttime observations in Capelle et al. (2022)] is applied. For A_{Theo} >1, the ΔT_5 difference remains unchanged while the standard deviation reduces from 0.38 to 0.36 K. In conclusion, if scenes containing aerosols are not frequent in the retained observations, aerosols may contribute to noise in our SST retrievals, but this effect is limited by the filtering applied on the DAOD. Finally, the quality of the results can be affected by errors on the input data used, such as those on the water vapor and temperature profiles, on the sea-surface emissivity, in particular for strong winds, and on the spectroscopy (i.e. water vapor continuum). Their impacts are however limited, as demonstrated by the sensitivity study in the Appendix of Capelle et al. (2022).

5. Conclusion and perspectives

We have shown that, even when solar light largely contributes to IASI radiances, the latter can be used for accurate sea-surface temperature (SST) retrievals, provided that a suitable physically-based radiative-transfer model is used. This is achieved, thanks to the availability of many mid-infrared channels, by fitting a wave-slope-probability dependent parameter which turns out to be in good agreement with direct theoretical predictions. The SSTs retrieved from numerous spectral channels in two windows centered near 3.7 and 4.0 μm are then very consistent and in excellent agreement with in-situ depth-temperature measurements after correction of the depth-to-skin difference. Indeed, the associated median biases are below 0.05 K with robust standard deviations lower than 0.35 K regardless of the solar contribution, even when the latter increases the observed brightness temperature by several tens of kelvin.

These results open renewed perspectives for the treatment of mid-infrared daytime radiances collected by hyperspectral sounders such as IASI, which are beyond the scope on this methodology paper but deserve investigation in the future. This is obviously the case for SST retrievals and the study of the diurnal cycle for which the radiances provided by IASI at 9:30 AM and 9:30 PM (local time at the Equator) could be complemented by those collected at other local times by hyperspectral sounders such as AIRS (Ruzmaikin et al., 2017), CrIS (Aumann et al., 2021), and potential future geostationary instruments. From this point of view, long time series may contribute to the still open issue (Ruzmaikin et al., 2017) of the Diurnal Temperature Range over seas. Perspectives are also opened, among others, for the exploitation of the information contained in the high frequency lines of the 4.3 μm CO_2 band [which are sensitive to both the temperature (Susskind et al., 2003 and 2010) and the CO_2 amount (Crevoisier et al., 2003) in the bottom part of the atmosphere], and the determination of atmospheric amounts of species, such as HDO (Herbin et al., 2009), showing signatures at high frequencies in IASI recordings. More generally, the optimal use of the mid-infrared region is among the priorities for future infrared sounders such as IASI-NG (Crevoisier et al., 2014).

Declaration of Competing Interest

The authors declare that they have no known competing financial interests or personal relationships that could have appeared to influence the work reported in this paper.

Acknowledgements

This work has been supported in part by CNRS, CNES and Ecole polytechnique. The authors acknowledge the IPSL mesocenter ESPRI facility for computer simulations, as well as EUMETSAT and the Aeris data infrastructure (https://www.aeris-data.fr/) for providing access to the IASI Level 1C data. They also thank Hugo Bellenger (from our laboratory) and Charles-Antoine Guérin (Institut Méditerranéen d'Océanologie, Toulon, France) for helpful discussions.

Appendices

Although some of the equations given below can be found in (or derived from) previously published papers (Masuda et al., 1988 ; Chen et al., 2013 ; Bréon, 1993 ; Bréon and Henriot, 2006 ; Cox and Munk, 1954), we reproduce them here in order to provide self-sufficient information to the reader.

Appendix A: The bidirectional reflectivity ρ

Since the (infrared) wavelengths used in this study are much smaller than all the spatial scales associated with the geometry of the sea surface, the reflection of solar radiation on the ocean is driven by the laws of geometrical optics. It is thus specular, and collecting along the $\vec{u}(\theta_I,\varphi_I)$ observation direction photons emitted by the sun along the $-\vec{u}(\theta_S,\varphi_S)$ vector (see Fig. 1) requires an ad hoc wave slope. The latter must have a normal vector $\vec{u}_\perp(\theta_I,\varphi_I,\theta_S,\varphi_S)$ along the direction defined by $\vec{u}(\theta_I,\varphi_I)+\vec{u}(\theta_S,\varphi_S)$. This unitary vector is, in the axis frame of Fig. 1, defined by the coordinates:

$$\vec{u}_\perp(\theta_I,\varphi_I,\theta_S,\varphi_S)=\begin{pmatrix}\sin(\theta_I)\cos(\varphi_I)+\sin(\theta_S)\cos(\varphi_S)\\ \sin(\theta_I)\sin(\varphi_I)+\sin(\theta_S)\sin(\varphi_S)\\ \cos(\theta_I)+\cos(\theta_S)\end{pmatrix}/N\,, \qquad \text{(A1)}$$

where $N = \sqrt{2+2\sin(\theta_I)\sin(\theta_S)\cos(\varphi_S-\varphi_I)+2\cos(\theta_S)\cos(\theta_I)}$. The angle of incidence $\theta_{Inc}(\theta_I,\varphi_I,\theta_S,\varphi_S)$ on the surface defined by this normal vector is such that:

$$\cos[\theta_{Inc}(\theta_I,\varphi_I,\theta_S,\varphi_S)]=\sqrt{\frac{1+\sin(\theta_I)\sin(\theta_S)\cos(\varphi_S-\varphi_I)+\cos(\theta_S)\cos(\theta_I)}{2}} \quad . \tag{A2}$$

The bidirectional reflectivity $\rho(\sigma,\theta_I,\varphi_I,\theta_S,\varphi_S)=\rho(\sigma,\theta_{Inc})$ can then be obtained using Fresnel's coefficients, Snell's law of refraction and the complex refractive index of sea water $n_{SW}(\sigma)$ as:

$$\rho(\sigma,\theta_{Inc})=[R_{//}^2(\theta_{Inc})+R_{\perp}^2(\theta_{Inc})]/2\,, \tag{A3}$$

with

$$\begin{aligned} R_{//}(\theta_{Inc}) &= -\frac{n_{SW}(\sigma)\cos(\theta_{Inc})-\cos[\theta_{Trans}(\theta_{Inc},\sigma)]}{n_{SW}(\sigma)\cos(\theta_{Inc})+\cos[\theta_{Trans}(\theta_{Inc},\sigma)]} \\ R_{\perp}(\theta_{Inc}) &= +\frac{\cos(\theta_{Inc})-n_{SW}(\sigma)\cos[\theta_{Trans}(\theta_{Inc},\sigma)]}{\cos(\theta_{Inc})+n_{SW}(\sigma)\cos[\theta_{Trans}(\theta_{Inc},\sigma)]} \end{aligned}, \tag{A4}$$

in which the spectrally-dependent angle $\theta_{Trans}(\theta_{Inc},\sigma)$ of the transmitted radiation is such that:

$$\sin[\theta_{Trans}(\theta_{Inc},\sigma)]=\sin(\theta_{Inc})/n_{SW}(\sigma) \quad . \tag{A5}$$

Note that, in the preceding equations, the index of refraction of air was (safely) replaced by unity.

Appendix B: Sensitivity of the retrieved SSTs to the input parameters

In Capelle et al. (2022), the sensitivity of SSTs retrieved in different windows of IASI spectra to various input parameters was studied. This included the influence of errors on the water vapor continuum parameterization, on the atmospheric water and temperature vertical profiles, and on the sea-surface emissivity. This analysis is thus not made here and the reader interested by this topic is invited to consult the appendices of Capelle et al. (2022). This previous analysis must here be complemented, since the treatment of daytime IASI spectra presented in this paper involves two new inputs: The solar spectrum and the bidirectional reflectivity (calculated from the index of refraction of water as described above).

It is obvious that any wavelength-independent scaling-factor error on the solar spectrum and/or reflectivity has no influence on the retrieved SSTs since it is automatically corrected through the adjustment of the solar parameter *A* (see Sec. 3.2 of the main text). In contrast, if the variations of the

relative error with σ within the spectral range used for the retrievals are wrong, this will impact the retrieved SST. In order to quantify this effect, we have reanalyzed all IASI spectra after applying a multiplicative factor $f(\sigma) = 1 + 0.01(\sigma - \bar{\sigma})/\Delta\sigma$ to the solar spectrum $I^0_{\mathrm{Sun}}(\sigma)$ in Eq. (8) of the main text [which is strictly equivalent to changing the bidirectional reflectivity $\rho(\sigma,\theta_I,\varphi_I,\theta_S,\varphi_S)$ by the same factor], where $\bar{\sigma} = 2620$ cm^{-1} and $\Delta\sigma$=280 cm^{-1}. This leaves the solar spectrum unchanged at the center of the range covered by windows W_4 and W_5 and changes it by +0.5 % (resp. -0.5 %) at the point of highest (resp. lowest) frequency.

Figure A1 displays the evolutions of the medians ΔTs retrieved in window W_5 using the original (Planck function at 5657 K) and modified [after applying the multiplicative factor $f(\sigma)$] solar spectra versus the solar parameter A_{Theo}. The difference observed between the two resulting ΔTs is proportional to A_{Theo}, with a coefficient of about 0.05. This shows that a perturbation of 1 % of the spectral dependence of either $I^0_{\mathrm{Sun}}(\sigma)$ or $\rho(\sigma,\theta_I,\varphi_I,\theta_S,\varphi_S)$ leads to a SST change of about 0.3 K for a large solar contribution corresponding to A_{theo}=6. This significant sensitivity of our results to such a perturbation implies that a careful choice of both $I^0_{\mathrm{Sun}}(\sigma)$ and $\rho(\sigma,\theta_I,\varphi_I,\theta_S,\varphi_S)$ must be made. From the literature, a large number of solar spectra are available [see references in Platnick et al. (2008) and in Coddington et al. (2019)]. Analysis of several of them shows that they involve spectral dependences differing from 1 to 3% when compared to the Planck function used here. The variability of the spectral dependence of $\rho(\sigma,\theta_I,\varphi_I,\theta_S,\varphi_S)$, linked to the uncertainties on the refractive index of sea water in the 3.6-4.0 μm region, seems to be less important. Indeed, comparing reflectivities computed from the data of Hale and Querry (1973) and of Downing and Williams (1975), for example, shows that the variation of the spectral dependence of $\rho(\sigma,\theta_I,\varphi_I,\theta_S,\varphi_S)$ is of about 0.3%. As shown by Fig. A1, any error on the spectral dependence of $I^0_{\mathrm{Sun}}(\sigma)$ and/or $\rho(\sigma,\theta_I,\varphi_I,\theta_S,\varphi_S)$ will cause, through their participations in Eq. (8), an artificial and wrong variation of the retrieved $\Delta T = T_{\mathrm{Skin}} - T_{\mathrm{Dept}}$ with A_{Theo}. It turns out that the choices we made, of a Planck function at T=5657 K for the sun radiance together with the refractive index of sea water from Downing and Williams (1975), lead to a pair with which the retrieved SSTs are, as they should be, practically independent of the solar contribution (i.e. of

A_{Theo}). Finally note that the black body temperature of 5657 K retained for the sun is that obtained, for the central wavelength (3.82 μm) of the interval used in this paper, using Eq. (6) of Platnick and Fontenla (2008) and that it leads to solar radiances within the uncertainties on the solar spectrum [which are discussed in Platnick and Fontenla (2008) and can be estimated from Fig. 1 of the same article].

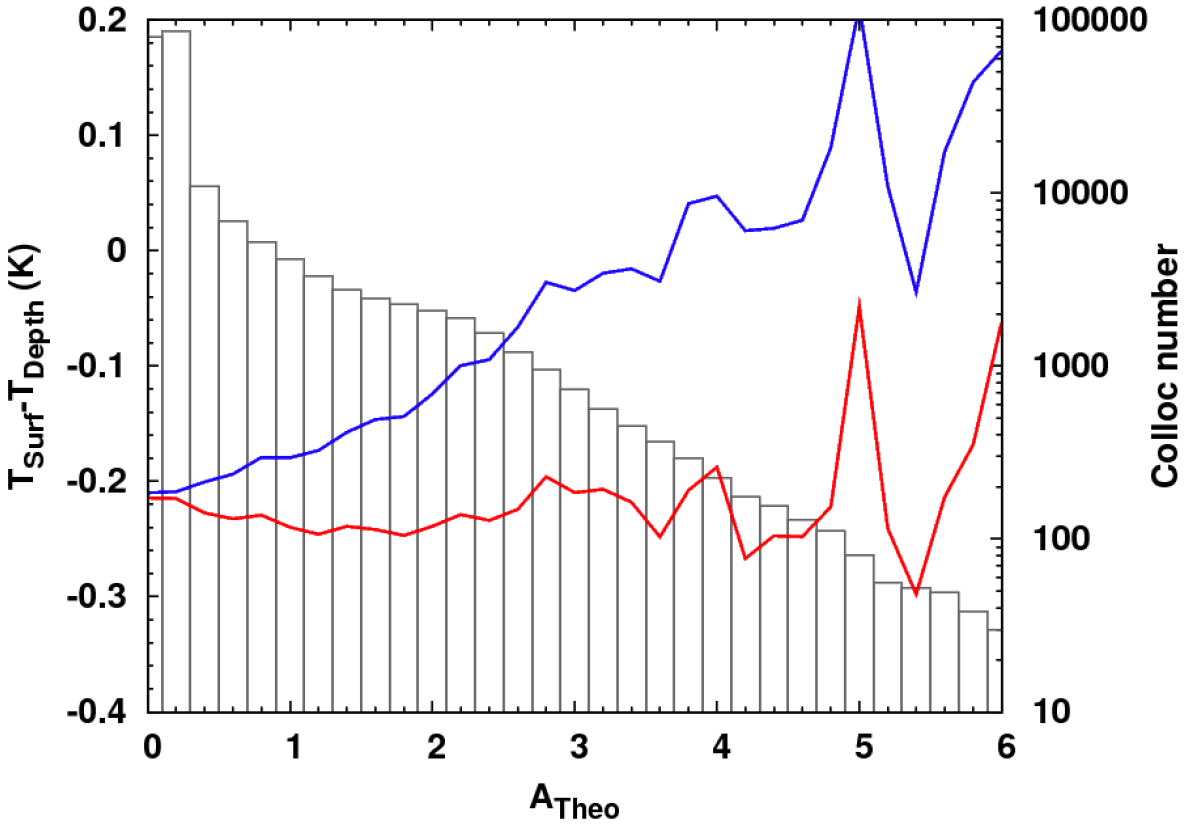

Figure A1: Left y axis: As in Figure 5 of the main text, average (over all observations using a bin of ΔA_{Theo}=0.2) differences $\Delta T_5 = \overline{T}_5 - T_{Depth}$ between the sea-surface skin temperatures retrieved from IASI spectra in window W_5 and the depth temperatures measured in situ, for the solar spectrum used in this study (Planck function at T=5657 K), in red, and after multiplying this function by a factor $f(\sigma) = 1 + 0.01(\sigma - \overline{\sigma})/\Delta\sigma$ (see text), in blue, versus the theoretical value A_{Theo} of the solar parameter computed (see Appendix C) using the parameterization of Bréon and Henriot (2006). The black line represents the values of ΔT computed for the conditions of each observation, following Fairall et al.

612 (1996), Wick et al. (2005) and Zeng and Beljaars (2005). Right y axis: Number of IASI-drifter
613 collocations used denoted by grey boxes in the figure.
614
615 **Appendix C: The solar parameter *A***
616 As explained in Appendix A, a reflecting wave with an ad hoc slope is needed for IASI to
617 collect photons coming from the sun, characterized by the vector $\vec{u}_{\perp}(\theta_I,\varphi_I,\theta_S,\varphi_S)$ [see Eq. (A1)]
618 orthogonal to its locally flat surface. The orientation of this surface is defined, in the axis frame of Fig.
619 1, by the slopes:

620
$$\frac{\partial z}{\partial x} = -\frac{\sin(\theta_S)\cos(\varphi_S)+\sin(\theta_I)\cos(\varphi_I)}{\cos(\theta_S)+\cos(\theta_I)}$$
$$\frac{\partial z}{\partial y} = -\frac{\sin(\theta_S)\sin(\varphi_S)+\sin(\theta_I)\sin(\varphi_I)}{\cos(\theta_S)+\cos(\theta_I)} \qquad \text{(A6)}$$

621 The probability $P(\partial z/\partial x,\partial z/\partial y)$ of waves to have these slopes was first investigated by Cox and
622 Munk (1954) with results confirmed later on by Bréon and Henriot (2006). Provided that the $\vec{x}$ axis is
623 chosen along the up-wind direction, both studies propose to parameterize this probability through:

624
$$P(\partial z/\partial x,\partial z/\partial y) = \frac{1}{2\pi\sigma_{//}\sigma_{\perp}}\exp\left[-\frac{\eta_{//}^2+\eta_{\perp}^2}{2}\right]\times\left[1-c_{21}(\eta_{\perp}^2-1)\eta_{//}/2-c_{03}(\eta_{//}^3-3\eta_{//})/6\right.$$
$$\left.+c_{40}(\eta_{\perp}^4-6\eta_{\perp}^2+3)/24+c_{04}(\eta_{//}^4-6\eta_{//}^2+3)/24+c_{22}(\eta_{//}^2-1)(\eta_{\perp}^2-1)/4\right]. \qquad \text{(A7)}$$
with $\eta_{//}\equiv\dfrac{\partial z/\partial x}{\sigma_{//}}$ and $\eta_{\perp}\equiv\dfrac{\partial z/\partial y}{\sigma_{\perp}}$

625 Values of $\sigma_{//}$, $\sigma_{\perp}$, c_{21}, c_{03}, c_{40}, c_{04}, and c_{22} have been given by Cox and Munk (1954) and by
626 Bréon and Henriot (2006), who parameterized them as a function of the wind speed at 12.5 m above
627 the sea surface. Note that since Eq. (A6) is obtained in the axis frame of Fig. 1, Eq. (A7) can only be
628 used after applying a change of $-\Delta\varphi$ to both φ_I and φ_S, where $\Delta\varphi$ is the angle between the (North-
629 South) $\vec{x}$ axis of Fig. 1 and the up-wind direction. Also recall that the angle $\theta_W(\theta_I,\varphi_I,\theta_S,\varphi_S)$
630 defining the wave tilt with respect to the horizontal is given by:

631
$$\mathrm{tg}(\theta_W)^2 = (\partial z/\partial x)^2+(\partial z/\partial y)^2 = \frac{\sin^2(\theta_S)+\sin^2(\theta_I)+2\sin(\theta_S)\sin(\theta_I)\cos(\varphi_S-\varphi_I)}{[\cos(\theta_S)+\cos(\theta_I)]^2}. \qquad \text{(A8)}$$

In order to go further and obtain the expression of $A(\theta_I,\varphi_I,\theta_S,\varphi_S)$, one must take into account the finite field of view of the IASI instrument and the wave-slope variations $\Delta(\partial z/\partial x)$ and $\Delta(\partial z/\partial y)$ associated with the solid angle within which radiation is collected. By using Eq. (A6) and changing variables using the Jacobian matrix of the derivatives of $\partial z/\partial x$ and $\partial z/\partial y$ with respect to θ_I and φ_I, one obtains (e.g.: Chen et al., 2013), after some (tedious) algebra and the removal of the IASI-viewing solid angle:

$$A_{\mathrm{Theo}}(\theta_I,\varphi_I,\theta_S,\varphi_S) = \frac{P(\theta_I,\varphi_I,\theta_S,\varphi_S)}{4\cos(\theta_S)\cos^4(\theta_W)} \ , \qquad \text{(A9)}$$

where θ_W is given by Eq. (A8).

For calculations of A_{Theo} using the above given equations, one must know the wind direction and speed at the (mast height) altitude of 12.5 m. Since we use data provided by the European Centre for Medium-Range Weather Forecasts' (ECMWF) 5th Re-Analysis (ERA5) dataset (Hersbach and Dee, 2016) at the altitude of 10 m, a correction was made using the log law, i.e. (Stull, 1988):

$$U(z) = \frac{U_*}{\kappa}\ln(z/z_0) \ , \qquad \text{(A10)}$$

where κ (=0.4) is the von Karmann constant, U_* is the friction velocity, and z_0 is the surface roughness length. The values of these last two parameters are obtained from knowledge of the wind speed $U(z_r)$ at a reference height z_r (here 10 m) by iteratively solving Eq. (A10) with z=z_r using the relations (Smith, 1988):

$$U_* = \frac{\kappa U(z_r)}{\ln(z_r/z_0)} \quad , \quad z_0 = \frac{0.11\nu}{U_*} + C\frac{U_*^2}{g} \ , \qquad \text{(A11)}$$

where ν (=0.14 cm^2.s) is the dynamic viscosity of air, g (=9.81 m/s^2) is the acceleration of gravity, and C (=0.018) is Charnook's constant. Note that, for the wind speeds at 10 m associated with the IASI observations treated in this study, which are all smaller than 20 m/s, the correction to 12.5 m is relatively small (less than +2.6 %).

Appendix D: The solar contribution

When very unlikely steep wave slopes are involved (e.g. when IASI looks in a direction opposite to that of the sun), the solar contribution to the collected radiances is small (see Fig. 3 of the main text). Such observations, which are close to nighttime conditions from the radiative point of view, are of little interest for the validation of the methodology proposed in this paper. In order to easily detect them, and more generally to quantify the solar contribution for the analysis of the results presented in Sec. 4.2, we have considered the difference $\overline{T}_5(A=0)-\overline{T}_5(A=A_{\mathrm{Fit}})$, between the average SST values retrieved in window W_5, without and with the solar contribution taken into account. The results, displayed in Fig. A2 below as a function of the theoretical value of A for each observation, demonstrate (as could be expected) a strong correlation, the mean value of $\overline{T}_5(A=0)-\overline{T}_5(A=A_{\mathrm{Fit}})$ for each A_{Theo} being well approximated, for $A_{\mathrm{Theo}}>0.5$ by $\overline{T}_5(A=0)-\overline{T}_5(A=A_{\mathrm{Fit}})\simeq 10+6(A_{\mathrm{Theo}}-0.5)$ K. Finally note that, $\overline{T}_5(A=0)$ and $\overline{T}_5(A=A_{\mathrm{Fit}})$ being averages over all spectral points in W_5 [see Eq. (9)], the values displayed in Fig. A2 can be significantly smaller than the difference $T(A=0,\sigma=\sigma_{\mathrm{Max}})-T(A=A_{\mathrm{Fit}},\sigma=\sigma_{\mathrm{Max}})$ obtained from the highest frequency (σ_{Max}=2760 cm^{-1}) of the IASI spectrum (see, Fig. 2 of the main text). It is here worth mentioning that an error of + 30 K on the SST retrieved, disregarding the solar contribution, from the IASI radiance at the highest wavenumber (2760 cm^{-1}), implies that the sun here participates for about 75% of the recorded signal !

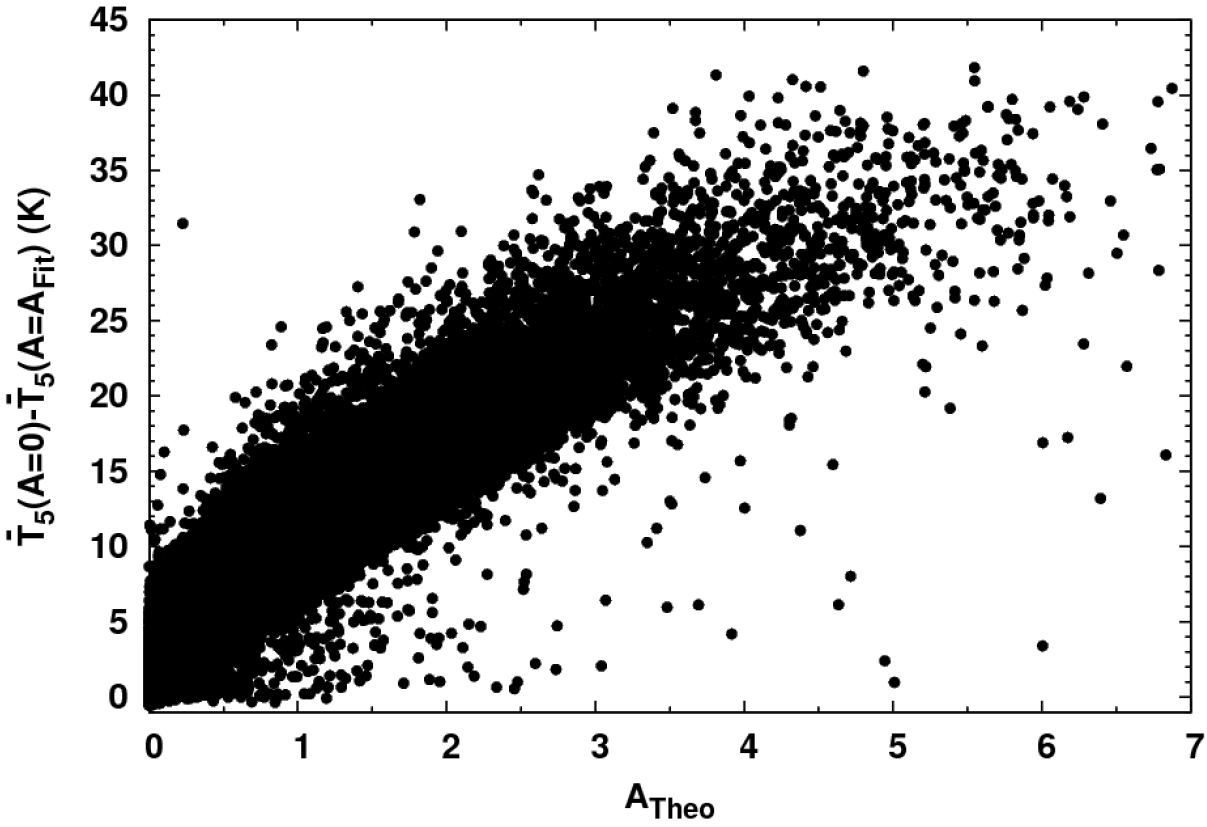

674

675 **Figure A2**: Differences, $\overline{T}_5(A=0)-\overline{T}_5(A=A_{\mathrm{Fit}})$, between the averaged SST values retrieved in window

676 W_5, without and with the solar contribution taken into account versus the theoretical value A_{Theo} of the solar

677 parameter computed using the parameterization of Bréon and Henriot (2006).

678

679

680 **References**

681 August, T., Klaes, D., Schlüssel, P., Hultberg, T., Crapeau, M., Arriaga, A., et al. (2012). IASI on
682 Metop-A: Operational Level 2 retrievals after five years in orbit. *J. Quant. Spectrosc. Radiat.*
683 *Transf.*, **113**, 1340-1371, https://doi.org/10.1016/j.jqsrt.2012.02.028

684 Aumann, H., Manning, E., Wilson, R. C., & Vazquez-Cuervo, J. (2021). Evaluation of AIRS and CrIS
685 SST Measurements Relative to Three Globally Gridded SST Products Between 2013 and 2019.
686 *IEEE Trans. Geosci. Remote Sens.*, **59**, 8094-8102, https://doi.org/10.1109/TGRS.2021.3052152

687 Bernie, D.J., Guilyardi, E., Madec, G., Slingo, J. M., & Woolnough, S. J. (2007). Impact of resolving
688 the diurnal cycle in an ocean–atmosphere GCM. Part 1: a diurnally forced OGCM. *Clim. Dyn.*, **29,**
689 575-590, https://doi.org/10.1007/s00382-007-0249-6
690 Bréon, F.-M., & Henriot, N. (2006). Spaceborne observations of ocean glint reflectance and modeling
691 of wave slope distributions. *J. Geophys. Res. (Oceans)*, **111**, C06005, doi:10.1029/2005JC003343
692 Bréon, F.-M. (1993). An analytical model for the cloud-free atmosphere/ocean system reflectance.
693 *Remote Sens. Environ.*, **43**, 179-182, https://doi.org/10.1016/0034-4257(93)90007-K
694 Capelle, V., Chédin, A., Péquignot, E., Schlüssel, P., Newman, S.M., & Scott, N.A. (2012). Infrared
695 continental surface emissivity spectra and skin temperature retrieved from IASI observations over
696 the tropics. *J. Appl. Meteorol. Climatol.*, **51**, 1164–1179. doi:10.1175/JAMC-D-11-0145.1
697 Capelle, V., Hartmann, J.-M., & Crevoisier, C. (2022). A full physics algorithm to retrieve nighttime
698 sea surface temperature with IASI: Toward an independent long time series. *Remote Sens.*
699 *Environ.*, **269**, 112838, https://doi.org/10.1016/j.rse.2021.112838
700 Chédin, A., Scott, N. A., Wahiche, C., & Moulinier, P. (1985). The improved initialization inversion
701 method: A high- resolution physical method for temperature retrievals from the TIROS-N series.
702 *J. Appl. Meteorol. Climatol.*, **24**, 128-143, doi:10.1175/1520-
703 0450(1985)024<0128:TIIIMA>2.0.CO;2
704 Chen, Y., Han, Y., van Delst, P., & Weng, F. (2013). Assessment of shortwave infrared sea surface
705 reflection and nonlocal thermodynamic equilibrium effects in the community radiative transfer
706 model using IASI data. *J. Atmos. Ocean. Techno.*, **30**, 2152-2160, https://doi.org/10.1175/JTECH-
707 D-12-00267.1
708 Cheruy, F., Scott, N. A., Armante, R., Tournier, B., & Chédin, A. (1995). Contribution to the
709 development of radiative transfer models for high spectral resolution observations in the infrared.
710 *J. Quant. Spectrosc. Radiat. Transf.*, **53**, 597-611, https://doi.org/10.1016/0022-4073(95)00026-H.
711 See also http://ara.abct.lmd.polytechnique.fr/index.php?page=4a
712 Chevallier, F. C., Chéruy, F., Scott, N. A., & Chédin, A. (1998). A Neural Network Approach for a
713 Fast and Accurate Computation of a Longwave Radiative Budget. *J. Appl. Meteorol. Climatol.*,
714 **37**, 1385–1397, doi:10.1175/1520-0450(1998)037<1385:annafa>2.0.co;2

715 Clayson, C. A., & Bogdanoff, A. S. (2013). The Effect of Diurnal Sea Surface Temperature Warming
716 on Climatological Air–Sea Fluxes. *J. of Climate*, **26**, 2546-2556. DOI:10.1175/JCLI-D-12-
717 00062.1
718 Coddington, O., Lean, J., Pilewskie, P., Snow, M., Richard, E., Kopp, G., et al. (2019). Solar
719 Irradiance Variability: Comparisons of Models and Measurements. *Earth Space Sci.*, **6**, 2525–
720 2555, doi:10.1029/2019EA000693
721 Cox, C., & Munk, W. (1954). Measurement of the roughness of the sea surface from photographs of
722 the Sun's glitter. *J. Opt. Soc. Am.,* **44**, 838-850, https://doi.org/10.1364/JOSA.44.000838
723 Crevoisier, C., Chédin, A., & Scott, N. A. (2003). AIRS channel selection for CO_2 and other trace-gas
724 retrievals. *Quart. J. Roy. Meteo. Soc.*, **129**, 2719-2740, https://doi.org/10.1256/qj.02.180
725 Crevoisier, C., Clerbaux, C., Guidard, V., Phulpin, T., Armante, R., Barret, B., et al. (2014). Towards
726 IASI-New Generation (IASI-NG): impact of improved spectral resolution and radiometric noise
727 on the retrieval of thermodynamic, chemistry and climate variables. *Atmos. Meas. Tech.,* **7***,* 4367-
728 4385, https://doi.org/10.5194/amt-7-4367-2014
729 DeSouza-Machado, S. G., Strow, L. L., Hannon, S. E., Motteler, H. E., Lopez−Puertas, M., Funke, B.,
730 et al. (2007). Fast forward radiative transfer modeling of 4.3 μm nonlocal thermodynamic
731 equilibrium effects for infrared temperature sounders. *Geophys. Res. Lett.*, **34**, L01802,
732 doi:10.1029/2006GL026684
733 Donlon, C. J., Minnett, P. J., Gentemann, C., Nightingale, T. J., Barton, I. J., Ward, B., et al. (2002).
734 Toward Improved Validation of Satellite Sea Surface Skin Temperature Measurements for
735 Climate Research. *J. of Climate*, **15**, 353-369, https://doi.org/10.1175
736 Downing, H.D., & Williams, D. (1975). Optical Constants of Water in the Infrared. *J. Geophys. Res.*,
737 **80**, 1656-1661, doi:10.1029/JC080i012p01656
738 Embury, O., Merchant, C.J., & Corlett, G.K., (2012). A reprocessing for climate of sea surface
739 temperature from the along-track scanning radiometers: initial validation, accounting for skin and
740 diurnal variability effects. *Remote Sens. Environ.*, **116**,62-78,
741 https://doi.org/10.1016/J.RSE.2011.02.028.

ECMWF (2016). IFS DOCUMENTATION – Cy43r1 Operational implementation 22 Nov 2016 PART IV: physical processes. Shinfield Park, Reading, RG2 9AX, England.

Fairall, C. W., Bradley, E. F., Godfrey, J. S., Wick, G. A., Edson, J. B., & Young, G. S. (1996). Cool-skin and warm-layer effects on sea surface temperature. *J. Geophys. Res. (Oceans)*, **101**, 1295-1308, https://doi.org/10.1029/95JC03190

Friedman, D. (1969). Infrared characteristics of ocean water (1.5-15 μ). *Appl. Opt.,* **8**, 2073-2078, https://doi.org/10.1364/AO.8.002073

Hale, G. M., & Querry, M. R. (1973). Optical constants of water in the 200-nm to 200-μm wavelength region. *Appl. Opt.,* **12**, 555-563, https://doi.org/10.1364/AO.12.000555

Hartmann, J.-M., Armante, R., Toon, G. C., Scott, N., Tran, H., Crevoisier, C., et al. (2018). Indirect influence of humidity on atmospheric spectra near 4 μm. *Geophys. Res. Lett.*, **45**, 12593– 12601, https://doi.org/10.1029/2018GL079582

Herbin, H., Hurtmans, D., Clerbaux, C., Clarisse, L., & Coheur, P.-F. (2009). $H_2{}^{16}O$ and HDO measurements with IASI/MetOp. *Atmos. Chem. Phys.*, **9**, 9433-9447, https://doi.org/10.5194/acp-9-9433-2009

Hersbach, H., & Dee, D. (2016). ERA5 reanalysis is in production. *ECMWF Newsletter* No. 147, 7. Available at https://www.ecmwf.int/en/newsletter/147/news/era5-reanalysis-production

Hersbach, H., Bell, B., Berrisford, P., Biavati, G., Horányi, A., Muñoz Sabater, J., et al. (2018). ERA5 hourly data on single levels from 1979 to present. Copernicus Climate Change Service (C3S) Climate Data Store (CDS). (Accessed on < 01-09-2020 >), available on https://cds.climate.copernicus.eu/ [WWW Document]. doi:10.24381/cds.adbb2d47

Hersbach, H., Bell, B., Berrisford, P., Hirahara, S., Horányi, A., Muñoz-Sabater, J., et al. (2020). The ERA5 global reanalysis. *Quart. J. Roy. Meteo. Soc.*, **146**, 1999–2049, doi:10.1002/qj.3803

Hilton, F., Armante, R., August, T., Barnet, C., Bouchard, A., Camy-Peyret, C., et al. (2012). Hyperspectral Earth observation from IASI: Five years of accomplishments. *Bull. Am. Meteo. Soc.*, **93**, 347-370, https://doi.org/10.1175/BAMS-D-11-00027.1. See also https://iasi.cnes.fr/en/IASI/index.htm

769 Jacquinet-Husson, N., Armante, R., Scott, N. A., Chédin, A., Crépeau, L., Boutammine, C., et al.
770 (2016). The 2015 edition of the GEISA spectroscopic database. *J. Mol. Spectrosc.*, **327**, 31-72,
771 https://doi.org/10.1016/j.jms.2016.06.007. See also https://geisa.aeris-data.fr/
772 Kawai, Y., & Wada, A. (2007). Diurnal sea surface temperature variation and its impact on the
773 atmosphere and ocean: A review. *J? Oceanogr.,* **63,** 721-744. https://doi.org/10.1007/s10872-007-
774 0063-0
775 Kilpatrick, K. A., Podestá, G., Walsh, S., Williams, E., Halliwell, V., Szczodrak, M., et al. (2015). A
776 decade of sea surface temperature from MODIS. *Remote Sens. Environ.*, **165**, 27-41,
777 https://doi.org/10.1016/j.rse.2015.04.023
778 Liang, X., Ignatov, A., Han, Y., & Zhang, H. (2010). Validation and improvements of daytime CRTM
779 performance using AVHRR IR 3.7 μm Band. *13th Conf. on Atmospheric Radiation*, 28 June-2 July
780 2010, Portland, USA. Available at https://ams.confex.com/ams/pdfpapers/170593.pdf
781 Liu, Q., Ignatov, A., Weng, F., & Liang, X. (2014). Removing Solar Radiative Effect from the VIIRS
782 M12 Band at 3.7 μm for Daytime Sea Surface Temperature Retrievals. *J. Atmos. Ocean.*
783 *Technol.*, **31**, 2522-2529. DOI:10.1175/JTECH-D-14-00051.1
784 López-Puertas, M., & Taylor, F. W. (2001). *Non-LTE radiative transfer in the atmosphere*. Series on
785 Atmospheric, Oceanic and Planetary Physics (Vol. 3). River Edge (NJ), World Scientific.
786 Martin, S. (2014). *An introduction to ocean remote sensing* (2nd Ed.). Cambridge, Cambridge
787 University Press.
788 Masuda, K., Takashima, T., & Takayama, Y. (1988). Emissivity of pure and sea waters for the model
789 sea surface in the infrared window regions. *Remote Sens. Environ.*, **24**, 313-329,
790 https://doi.org/10.1016/0034-4257(88)90032-6
791 Masuda, K. (2008). Dependence of sea surface emissivity on temperature-dependent refractive index.
792 *Quart. J. Roy. Meteo. Soc.*, **134**, 541-545, https://doi.org/10.1002/qj.192
793 Merchant, C. J., Llewellyn-Jones, D., Saunders, R. W., Rayner, N. A., Kent, E. C., Old, C. P., et al.
794 (2008). Deriving a sea surface temperature record suitable for climate change research from the
795 along-track scanning radiometers. *Adv. Space Res.*, **41**, 1-11, doi:10.1016/J.ASR.2007.07.041

796 Merchant, C. J., Harris, A. R., Roquet, H., & Le Borgne, P. (2009a). Retrieval characteristics of non-
797 linear sea surface temperature from the advanced very high resolution radiometer. *Geophys. Res.*
798 *Lett.*, **36**, 1-5. https://doi.org/10.1029/2009GL039843
799 Merchant, C. J., Harris, A. R., Maturi, E., Embury, O., MacCallum, S. N., Mittaz, J., & Old, C. P.
800 (2009b). Sea Surface Temperature Estimation from the Geostationary Operational Environmental
801 Satellite-12 (GOES-12). *J. Atmos. Ocean. Technol.,* **26**, 570-581,
802 https://doi.org/10.1175/2008JTECHO596.1
803 Merchant, C.J., Embury, O., Rayner, N.A., Berry, D.I., Corlett, G.K., Lean, K., et al. (2012). A 20
804 year independent record of sea surface temperature for climate from Along-Track Scanning
805 Radiometers. *J. Geophys. Res.* (Ocean), **117**, 1-18. doi:10.1029/2012JC008400
806 Merchant, C. J., Embury, O., Bulgin, C. E., Block, T., Corlett, G. K., Fiedler, E., et al. (2019).
807 Satellite-based time-series of sea-surface temperature since 1981 for climate applications. *Sci.*
808 *Data,* **6**, article # 223, https://doi.org/10.1038/s41597-019-0236-x
809 Minnett, P. J., Smith, M., & Ward, B. (2011). Measurements of the oceanic thermal skin effect. *Deep*
810 *Sea Res. Part II: Topical Studies in Oceanography*, **58**, 861-868,
811 https://doi.org/10.1016/j.dsr2.2010.10.024
812 Minnett, P. J., & Corlett, G. K. (2012). A pathway to generating Climate Data Records of sea-surface
813 temperature from satellite measurements. *Deep Sea Res. Part II: Topical Studies in*
814 *Oceanography*, **77-80**, 44-51, doi:10.1016/j.dsr2.2012.04.003
815 Minnett, P. J., Alvera-Azcárate, A., Chin, T. M., Corlett, G. K., Gentemann, C. L., Karagali, I., et al.
816 (2019). Half a century of satellite remote sensing of sea-surface temperature. *Remote Sens.*
817 *Environ.*, **233**, 111366, https://doi.org/10.1016/j.rse.2019.111366
818 Mlawer, E. J., Payne, V. H., Moncet, J., Delamere, J. S., Alvarado, M. J., & Tobin, D. C. (2012).
819 Development and recent evaluation of the MT_CKD model of continuum absorption. *Phil. Trans.*
820 *Roy. Soc. A*, **370**, 2520-2556, https://doi.org/10.1098/rsta.2011.0295. The current version of the
821 MT_CKD water vapor continua can be found at http://rtweb.aer.com/continuum_frame.html

822 Morak-Bozzo, S., Merchant, C.J., Kent, E.C., Berry, D.I., & Carella, G. (2016), Climatological diurnal
823 variability in sea surface temperature characterized from drifting buoy data. *Geosci. Data J.*, **3**, 20-
824 28. https://doi.org/10.1002/gdj3.35
825 Nayar, K. G., Sharqawy, M. H., Banchik, L. D., & Lienhard V, J. H. (2016). Thermophysical
826 properties of seawater: A review and new correlations that include pressure dependence.
827 *Desalination,* **390**, 1-24, doi:10.1016/J.DESAL.2016.02.024
828 Newman, S. M., Smith, J. A., Glew, M. D., Rogers, S. M., & Taylor, J. P. (2005). Temperature and
829 salinity dependence of sea surface emissivity in the thermal infrared. *Quart. J. Roy. Meteo. Soc.*,
830 **131**, 2539-2557, https://doi.org/10.1256/qj.04.150
831 O'Carroll, A. G., August, T., Le Borgne, P., & Marsouin, A. (2012) The accuracy of SST retrievals
832 from Metop-A IASI and AVHRR using the EUMETSAT OSI-SAF matchup dataset. *Remote Sens.*
833 *Environ.*, **126**, 184-194, https://doi.org/10.1016/j.rse.2012.08.006
834 Ohring, G., Wielicki, B., Spencer, R., Emery, B., & Datla, R., 2005. Satellite instrument calibration
835 for measuring global climate change: Report of a workshop. *Bull. Am. Meteo. Soc.*, **86**, 1303-
836 1313, doi:10.1175/BAMS-86-9-1303
837 Peyridieu, S., Chédin, A., Capelle, V., Tsamalis, C., Pierangelo, C., Armante, R., Crevoisier, C.,
838 Crépeau, L., Siméon, M., Ducos, F., & Scott, N.A. (2013). Characterisation of dust aerosols in the
839 infrared from IASI and comparison with PARASOL, MODIS, MISR, CALIOP, and AERONET
840 observations. *Atmos. Chem. Phys.,* **13**, 6065-6082. doi:10.5194/acp-13-6065-2013
841 Pierangelo, C., Chédin, A., & Legrand, M. (2013). Longwave passive remote sensing. In: Lenoble, J.,
842 Remer, L., Tanre, D. (eds) Aerosol Remote Sensing. Springer, Berlin, Heidelberg.
843 https://doi.org/10.1007/978-3-642-17725-5_9
844 Platnick, S., & Fontenla, J. M. (2008). Model Calculations of Solar Spectral Irradiance in the 3.7-μm
845 Band for Earth Remote Sensing Applications, *J. Appl. Meteorol. Climatol.*, **47**, 124-134,
846 https://doi.org/10.1175/2007JAMC1571.1
847 Robinson, L. S. (2010). *Discovering the ocean from space*. Berlin Heidelberg, Springer-Verlag.
848 Rousseeuw, P. J., & Hubert, M. (2011). Robust statistics for outlier detection. *Wiley Interdiscip. Rev.*
849 *Data Min. Knowl. Discov.*, **1**, 73-79. DOI: 10.1002/widm.2

Ruzmaikin, A., Aumann, H. H., Lee, J., & Susskind, J. (2017). Diurnal cycle variability of surface temperature inferred from AIRS data. *J. Geophy. Res. (Atmospheres)*, 122, 10,928- 10,938. https://doi.org/10.1002/2016JD026265

Saunders, P. M. (1967). The temperature at the ocean-air interface. *J. Atmos. Sci.*, **24**, 269-273, https://doi.org/10.1175/1520-0469(1967)024<0269:TTATOA>2.0.CO;2

Scott, N. A., & Chédin, A. (1981). A fast line-by-line method for atmospheric absorption computations: The automatized atmospheric absorption atlas. *J. Appl. Meteorol. Climatol.,* **20**, 802-812, https://doi.org/10.1175/1520-0450(1981)020<0802:AFLBLM>2.0.CO;2

Serio, C., Masiello, G., Camy-Peyret, C., Jacquette, E., Vandermarcq, O., Bermudo, F., et al. (2018). PCA determination of the radiometric noise of high spectral resolution infrared observations from spectral residuals: Application to IASI. *J. Quant. Spectrosc. Radiat. Transf.*, **206**, 8-21, https://doi.org/10.1016/j.jqsrt.2017.10.022

Sharqawy, M. H., Lienhard V, J. H., & Zubair, S.M. (2010). Thermophysical properties of seawater: a review of existing correlations and data. *Desalination Water Treat.*, **16**, 354–380, doi:10.5004/dwt.2010.1079

Smith, S. D. (1988). Coefficients for sea surface wind stress, heat flux, and wind profiles as a function of wind speed and temperature, *J. Geophys. Res. (Oceans)*, **93**, 15467-15472, doi:10.1029/JC093iC12p15467

Stuart-Menteth, A. C., Robinson, I. S., & Challenor, P. G. (2003), A global study of diurnal warming using satellite-derived sea surface temperature, *J. Geophys. Res.*, **108**, 3155, doi:10.1029/2002JC001534

Stull, R. B. (1988). *An introduction to boundary layer meteorology*. Dordrecht, Kluwer.

Susskind, J., Barnet, C., & Blaisdell, J. (2003). Retrieval of atmospheric and surface parameters from AIRS/AMSU/HSB data in the presence of clouds. *IEEE Trans. Geosci. Remote Sens.*, **41**, 390-409, https://doi.org/10.1109/TGRS.2002.808236

Susskind, J., Blaisdell, J. & Iredell, L. (2010). Improved determination of surface and atmospheric temperatures using only shortwave AIRS channels: the AIRS version-6 retrieval algorithm. *IEEE*

877 *International Geoscience and Remote Sensing Symposium*, Honolulu, HI, 2010, pp. 2948-2951.
878 Available at https://ieeexplore.ieee.org/stamp/stamp.jsp?tp=&arnumber=5650538
879 Tsamalis, C., & Saunders, R. (2018).Quality Assessment of Sea Surface Temperature from ATSRs of
880 the Climate Change Initiative (Phase 1). *Remote Sens.*, **10**, 497.
881 https://doi.org/10.3390/rs10040497
882 Turner, D.S. (2004). Systematic errors inherent in the current modeling of the reflected downward flux
883 term used by remote sensing models. *Appl. Opt.*, **43**, 2369-2383, doi:10.1364/ao.43.002369
884 Walton, C. C., Pichel, W. G., Sapper, J. F., & May, D. A. (1998). The development and operational
885 application of nonlinear algorithms for the measurement of sea surface temperatures with the
886 NOAA polar-orbiting environmental satellites. *J. Geophys. Res. (Oceans)*, **103**, 27999-28012,
887 https://doi.org/10.1029/98JC02370
888 Watts, P. D., Allen, M. R., & Nightingale, T. J. (1996). Wind Speed Effects on Sea Surface Emission
889 and Reflection for the Along Track Scanning Radiometer. *J. Atmos. Ocean. Technol.*, **13**, 126-141.
890 DOI:10.1175/1520-0426(1996)013<0126:WSEOSS>2.0.CO;2
891 Wick, G. A., Ohlmann, J. C., Fairall, C. W., & Jessup, A. T. (2005). Improved oceanic cool-skin
892 corrections using a refined solar penetration model. *J. Phys. Oceano.*, **35**, 1986-1996,
893 doi:10.1175/JPO2803.1
894 Xu, F., & Ignatov, A. (2014). In situ SST Quality Monitor (iQuam). *J. Atmos. Ocean. Techno.*, **31**,
895 164-180, https://doi.org/10.1175/JTECH-D-13-00121.1
896 Zeng, X., & Beljaars, A. (2005). A prognostic scheme of sea surface skin temperature for modeling
897 and data assimilation. *Geophys. Res. Lett.*, **32**, 1-4, doi:10.1029/2005GL023030
898 Zhang, H., & Wang, M. (2010). Evaluation of sun glint models using MODIS measurements.
899 *J. Quant. Spectrosc. Radiat. Transf.*, **111**, 492-506, https://doi.org/10.1016/j.jqsrt.2009.10.001
900 Yu, H., Tan, Q., Chin, M., Remer, L.A.L.A., Kahn, R.A.R.A., Bian, H., Kim, D., Zhang, Z., Yuan, T.,
901 Omar, A.H.A.H., Winker, D.M.D.M., Levy, R.C.R.C., Kalashnikova, O., Crepeau, L., Capelle, V.,
902 Chédin, A., Kahn, A., Kalashnikova, O., Crepeau, L., Capelle, V., & Chédin, A. (2019). Estimates
903 of African Dust Deposition Along the Trans-Atlantic Transit Using the Decadelong Record of

Aerosol Measurements from CALIOP, MODIS, MISR, and IASI. *J. Geophys. Res. Atmos.*, **124**, 1–47. doi:10.1029/2019JD030574